AIAA JOURNAL
Vol. 60, No. 9, September 2022

Calibration of the Critical Amplification Factor for Reynolds-Averaged Navier–Stokes-Based Transition Modeling

Reza Djeddi,* James G. Coder,† and Kivanc Ekici‡
University of Tennessee, Knoxville, Tennessee 37996

https://doi.org/10.2514/1.J061476

The present study uses an adjoint-based gradient optimization framework to perform calibration of the critical amplification factor for transition models based on the linear stability theory. More specifically, the two-equation amplification factor transport model is used, and the critical amplification factor, which directly controls the onset of the transition via the source term of the intermittency equation, is calibrated for a set of canonical flat plate test cases in both bypass and natural transitional regimes. It is shown that, by utilizing a sigmoid fitting of the turbulence index profile, the transition onset location can be accurately predicted in a differentiable and smooth fashion, which is essential to the adjoint-based sensitivity analysis of the Reynolds-averaged Navier–Stokes solver. Subsequently, the results of these calibration studies are used for obtaining a new relation via a high-order polynomial regression model relating the critical amplification factor to the freestream turbulence intensity. Finally, the prediction capability of the calibrated relation is tested for natural transitional flows past NLF(1)-0416 and S809 airfoils. The numerical results show significant improvements in predicting the transition onset location as well as lift and drag predictions.

Nomenclature

C_D, C_L	=	drag and lift coefficients
C_f	=	skin friction coefficient
c	=	chord length
E	=	total energy per unit mass
H_L	=	local boundary-layer shape factor
I	=	objective function
i_t	=	turbulence index (Spalart–Allmaras model)
L	=	reference length
M_∞	=	freestream Mach number
$\tilde{n}$	=	modified amplification factor (amplification factor transport model)
Pr	=	Prandtl number
p	=	pressure
$\mathcal{R}$	=	residual of state variables
Re	=	Reynolds number
$S, \tilde{S}$	=	original and limited/clipped magnitude of strain rate tensor
u, v, w	=	Cartesian velocity components
x, y, z	=	Cartesian coordinates
y^+	=	nondimensional distance from the first cell to the wall
α	=	angle of attack
$\gamma, \tilde{\gamma}$	=	original and modified intermittency
μ	=	dynamic viscosity
ν	=	kinematic viscosity (i.e., viscous diffusivity)
$\tilde{\nu}$	=	modified eddy viscosity (Spalart–Allmaras model)
ρ	=	density
τ	=	shear stress
$\sigma, \sigma_n, \sigma_\gamma$	=	turbulent Prandtl number (Spalart–Allmaras model) and its variants in the amplification factor transport model
χ	=	eddy viscosity ratio (Spalart–Allmaras model)
Ω	=	vorticity magnitude

Presented as Paper 2021-3036 at the AIAA Aviation 2021 Forum, Virtual Event, August 2–6, 2021; received 22 November 2021; revision received 25 April 2022; accepted for publication 8 May 2022; published online 27 May 2022.

*Research Assistant Professor and Lecturer; sdjeddi@vols.utk.edu. Professional Member AIAA (Corresponding Author).
†Assistant Professor. Senior Member AIAA.
‡Professor, Mechanical, Aerospace, and Biomedical Engineering. Senior Member AIAA.

I. Introduction

LAMINAR-TO-TURBULENT transition of boundary layers is of utmost relevance in aerodynamic applications involving commercial aircraft, rotorcraft, turbomachinery, and wind turbines. Accurate prediction of the transition onset directly impacts the boundary-layer development, flow separation, friction drag count, and maximum lift coefficient, all of which significantly influence the overall design and performance of the aerodynamic body. While it is generally common for Reynolds-averaged Navier–Stokes (RANS) simulations to be run in a fully turbulent mode, ignoring transition prediction in computational fluid dynamics (CFD) analyses involving flows dominated by laminar regime can significantly reduce the accuracy and reliability of these studies. Several factors, such as freestream turbulence intensity (FSTI), pressure gradients, and surface roughness, can trigger boundary-layer instabilities that would eventually lead to "tripping" or transition phenomenon. Unlike many earlier approaches that rely on purely empirical local correlations for transition prediction, the linear stability theory has given way to a new class of phenomenological techniques that offer a more physics-based approach to predicting transition. As an example, the e^N method of Smith [1] and van Ingen [2], which is based on the linear stability theory, assumes that transition occurs when the maximum amplification factor of any boundary-layer instability reaches or exceeds a prespecified value N_{crit}. This critical amplification factor was originally taken to be nine, i.e., an amplification ratio of $e^9 \approx 8100$, for standard aerodynamic problems in low-turbulence conditions. It was later extended by Mack [3] to account for varying freestream turbulence intensities based on available experimental data.

An in-depth uncertainty quantification and sensitivity analysis of the AFT transition model was presented by the authors in an earlier work [4] involving several bypass and natural transitional benchmark test cases. It was shown that, for these canonical problems, the sensitivities of the closure coefficients of the AFT model have opposite signs. This can result in an ill-posed optimization problem with the goal of obtaining a global or universal set of optimal closure coefficients via a multipoint transition onset calibration. Therefore, in

this work, the critical amplification factor is calibrated using canonical flat plate test cases in both bypass and natural transitional regimes.

It is important to note that the underlying theory of the AFT model is based on the linear instability growth, which is generally assumed relevant only when the FSTI is less than 1% (natural transition). From the model development standpoint, however, the proposed approach in our work offers continuity between bypass and natural transitional flow regimes. While for low FSTI values the model is anchored by physics, which might not be the case for very high FSTI value, it is still possible to obtain useful results in bypass transitional region (with high FSTI or very low critical amplification factors). Additionally, it is worth noting that most widely used Partial Differential Equations (PDE) based (such as the Langtry–Menter [5] or Menter–Smirnov [6]) or algebraic (such as Bas-Cakmakcioglu (B-C) [7]) transition models are purely empirical and do not have strong traceability to physical arguments. For example, the Langtry–Menter [5] model does not rely on the exponential growth of Tollmien–Schlichting waves, which are the main driver for transition in natural regimes. Also, the Langtry–Menter transition model, originally developed to complement the Shear Stress Transport (SST) turbulence model [8], utilizes a locally estimated length scale described as a function of the pressure gradient and the turbulence intensity at the edge of the boundary layer, Tu_e. As such, bypass transitional cases at high freestream turbulence intensities can be handled by the Langtry–Menter model by focusing on the changes in Tu_e rather than the freestream turbulence intensity Tu_∞. However, in this work, the Spalart–Allmaras (SA) turbulence model [9] is used where the Tu_e information is not available. Therefore, utilizing the freestream turbulence intensity Tu_∞ to determine the critical amplification factor is the only option. At the same time, the use of the proposed technique allows us to completely eliminate the need for a case-by-case or manual calibration of the model parameters, specifically the critical amplification factor. The critical amplification factor N_{crit} in the AFT transition model plays a significant role in the prediction of the transition onset. On the other hand, many research studies in the literature that focus on transition prediction using the correlation-based transition models reportedly modify the freestream turbulence intensity, which sets the critical amplification factor through Mack's relation, from its experimentally calculated value in order to reduce the discrepancies between CFD and experimental results [7,10,11]. Therefore, using our proposed strategy, it would be no longer necessary to tune the N_{crit} parameter in order to match the experimental data for all FSTI values ranging from bypass to natural transitional flow regimes.

It must be noted that the critical amplification factor N_{crit} controls the onset of the transition via the source term of the intermittency equation, and our numerical results have shown a significant improvement in the transition prediction accuracy when this critical factor is calibrated. Ultimately, the results of the calibration studies for the critical amplification factor are used in determining a new relation, similar to that of Mack [3] and Drela [12] that determines the value of the critical factor as a function of the freestream turbulence intensity. The efficacy of the calibrated relation is tested for two airfoil cases (cf. Ref. [13]), NLF(1)-0416 and S809, subject to natural transitional flows. Our numerical results have shown a significant improvement in the transition onset location as well as lift and drag predictions by utilizing the calibrated critical amplification factor for these natural transitional cases. To the best of the authors' knowledge, this is the first attempt to calibrate the critical amplification factor using a gradient-based optimization based on the discrete adjoint form of the RANS equations.

II. Mathematical Formulation

In this section, details of the amplification factor transport (AFT) transition model as well as the SA turbulence model are presented. Moreover, numerical considerations for "smoothing" the transition model are presented to enable the gradient-based design optimization aimed at calibrating the closure coefficients of the AFT model as well as the critical amplification factor. Additionally, the coupling of the transition and turbulence models is described, and numerical details of the calibration design problem are presented.

A. Transition Modeling Equations

The basis for the AFT transition model is the solution of a surrogate variable $\tilde{n}$, called the modified amplification factor, which characterizes the envelope of linearly amplified instabilities throughout the boundary layer. The main advantage of the AFT model that sets it apart from other widely used transition models is that it is built on the premise that integral boundary-layer (IBL) quantities, such as the shape factor, are estimated using local surrogates. This estimation process relies on the carefully guided calibration of the AFT model closure coefficients based on the fundamental boundary-layer theory. Details of the additional transport equations solved for the AFT model are presented in the following sections.

1. Amplification Factor Transport

Originally developed by Coder and Maughmer [14], the AFT model focuses on solving a transport equation for the approximate envelope amplification factor such that

$$\frac{\partial \rho \tilde{n}}{\partial t} + \underbrace{\frac{\partial \rho u_j \tilde{n}}{\partial x_j}}_{\text{convective flux}} - \underbrace{\frac{\partial}{\partial x_j}\left[\sigma_n(\mu + \mu_t)\frac{\partial \tilde{n}}{\partial x_j}\right]}_{\text{diffusive flux}} = \underbrace{\rho \Omega F_{\text{crit}} F_{\text{growth}} \frac{d\tilde{n}}{dRe_\theta}}_{\text{source term}} \tag{1}$$

Details of the AFT transition model are presented in Ref. [15] as well as an earlier work by authors [4]. However, definitions for some of the individual terms in the governing equations of the AFT model will be presented in this section. As discussed earlier, the boundary-layer methods rely on the availability of the integral momentum thickness as well as the integral shape factor to determine the boundary-layer profile. However, the AFT model focuses on estimating the integral properties using a *local shape factor*. This local shape factor that was originally proposed in the AFT2017a model [16] is defined as

$$H_L = \frac{d^2}{\mu}[\nabla(\rho \boldsymbol{u} \cdot \nabla d) \cdot \nabla d] \tag{2}$$

where d is the shortest distance from wall, and the gradient of the wall distance in Eq. (2) is a reflection of the wall-normal derivative of the wall-normal momentum as a Galilean-invariant indicator of streamwise velocity gradient. Additionally, one of the most important terms in the AFT equation is a step function called F_{crit}, which toggles from 0 to 1 as a function of the local vorticity Reynolds number. The value of the critical function becomes 1 when the local vorticity Reynolds number reaches a critical threshold $Re_{\nu,0}$, which is correlated to the transition momentum-thickness Reynolds number by a function of the integral shape factor H_{12} [15,17]. Note that the step function described above is nonsmooth and nondifferentiable at $Re_\nu = Re_{\nu,0}$, which will be the focus of the smoothing procedure that will be described later in this work. This smoothing process would be essentially important in order to enable gradient-based calibration involving the AFT transition model.

2. Intermittency Transport

Unlike the earlier versions of the AFT model, i.e., AFT2014 [14] and AFT2017a [16], where an algebraic intermittency was being used for suppressing turbulence production in the laminar boundary layers, the AFT2017b [18] and, later, the AFT2019 [15] versions utilized a transport equation for the modified intermittency $\tilde{\gamma}$, which is a mapping of the actual intermittency γ values of 0 in laminar regions but 1 in turbulent regimes [5]. As was also done in an earlier work [4], a slightly modified version of the AFT2019 transition model is utilized herein where we solve the transport equation (second governing equation of the AFT model) for the actual intermittency instead, which makes the transport equation identical to that of Menter et al. [6]. It must be noted that, in the original AFT2019 version, the modified intermittency $\tilde{\gamma}$ was introduced in order to allow for the implementation of the model in finite-element solvers that

often require variables to have physical interpretations at both positive and negative values [15]. Moreover, the use of the modified intermittency function yields a nonlinear diffusion term that was omitted for simplicity in all previous AFT model implementations, although numerical studies across a variety of cases indicated a negligible impact for this nonlinear term [15]. In this work, however, the original intermittency transport equation is utilized instead since our numerical results have also shown a slightly improved convergence behavior and stability for our fully coupled finite-volume RANS solver. As such, the intermittency transport equation is described below:

$$\frac{\partial \rho\gamma}{\partial t} + \underbrace{\frac{\partial \rho u_j \gamma}{\partial x_j}}_{\text{convective flux}} - \underbrace{\frac{\partial}{\partial x_j}\left[\left(\mu + \frac{\mu_t}{\sigma_\gamma}\right)\frac{\partial \gamma}{\partial x_j}\right]}_{\text{diffusive flux}} = \underbrace{c_1 \rho S F_{\text{onset}}(1-\gamma)}_{\text{production source term}} - \underbrace{c_2 \rho \Omega F_{\text{turb}}(c_3\gamma - 1)}_{\text{destruction source term}} \quad (3)$$

Both the F_{onset} and F_{turb} functions in the production and destruction source terms of the intermittency equation use minimum and maximum functions that can be locally nondifferentiable. Additionally, the F_{onset} function relies on the $\tilde{n}/\mathrm{N}_{\text{crit}}$ ratio, which is a balance between the local approximate envelope amplification factor and a critical value in order to determine the onset of transition. Here, N_{crit} is the critical amplification factor based on the linear stability theory [15], which will be described later.

Ultimately, the destruction source term of the intermittency equation is controlled by the F_{turb} function to prevent destruction of intermittency within an already turbulent boundary layer based on the value of R_T. As a matter of fact, F_{turb} promotes laminarization in boundary layers with small turbulence Reynolds number while maintaining intermittency in turbulent boundary layers with large values of R_T. It is very important to note that F_{turb} can in some cases inadvertently suppress the turbulence in the viscous sublayer due to the local nature of the turbulent Reynolds number. However, this issue is handled primarily by the turbulence model, and the details of this will be described later in this work when the turbulence and transition models are coupled together. Another important issue to address is the number of minimum and maximum functions in the definition of the intermittency source term. These functions are also nonsmooth and nondifferentiable at their inflection point, which will be addressed in the following section.

3. Smooth Version of the AFT Model

As discussed earlier in the definition of the original AFT model, the switching step function as well as the minimum and maximum functions are nonsmooth and discontinuous. This means that these functions must be modified in order to smooth the AFT model and make it compatible with the gradient-based design optimization. The first function that will be addressed is the F_{crit} step function, which is substituted by a modified hyperbolic tangent function [4,19]. Additionally, the minimum and maximum functions must be made smooth as these functions are used substantially in the calculation of the source terms for both of the AFT model equations. Moreover, the minimum and maximum functions are also used in the turbulence model, and smoothing them would be essentially important for the compatibility of these models with gradient-based design optimization. In this work, the Kreisselmeier–Steinhauser (KS) function [20,21] is used to smooth the minimum and maximum functions. It must be noted that the KS functions are used to smooth the min and max functions that arise in various mathematical applications involving a series of *measure* functions.

4. Critical Amplification Factor

In the Langtry–Menter transition model [5], the value of the freestream turbulence intensity is used to determine the critical momentum-thickness Reynolds number $Re_{\theta,c}$ through special correlations, such as Abu-Ghannam/Shaw criterion [22], to determine the onset of transition. It must be noted that these correlations have been carefully calibrated for various test cases based on the experimental results, and there is ongoing research in this area to improve such correlations [23–25]. In the AFT transition model, however, the FSTI is used for determining the critical amplification factor N_{crit} that directly controls the onset function in the source term of the intermittency equation. This critical factor is directly related to the freestream turbulence intensity according to the modified [12] Mack's relationship [3]:

$$N_{\text{crit}} = -8.43 - 2.4\,\ell_n\left(\frac{\tau}{100}\right)$$
$$\tau = 2.5\,\tanh\left(\frac{Tu\%}{2.5}\right) \quad (4)$$

where τ is a smooth maximum function designed for preserving the positive values of the critical amplification factor, and $Tu\%$ is the freestream turbulence intensity described in percent value.

It is important to note that the freestream turbulence intensity is defined as the ratio of the standard deviation of the mean velocity to the mean velocity (commonly reported in percent value). Therefore, in many experimental studies and wind tunnel data, the value of the FSTI (or Tu_∞) is calculated very accurately by relying on freestream velocity data typically measured using a constant temperature anemometer (CTA) [26] or laser velocimeters [27]. On the other hand, in many RANS-based transition prediction studies, the discrepancies between the CFD solutions and the experimental data are normally alleviated by manually tuning the turbulence intensity (FSTI) [7,10,11,19,28,29]. In the case of the transition models based on the linear stability theorem, e.g., the e^N or the AFT models [15,28,30], this variation of the FSTI value is analogous to the variations of the critical amplification factor N_{crit}. It is worth noting that the linear stability theory that governs the AFT model is generally assumed relevant for $Tu_\infty < 1\%$ (natural transition) regimes, which means that for low FSTI values the model is anchored by physics. However, as mentioned earlier, it is still possible to obtain useful results in bypass transitional region [31]. On the other hand, the Langtry–Menter [5] model utilizes calibrated correlations for the local transition momentum-thickness Reynolds number as a function of the pressure gradient and the turbulence intensity at the edge of the boundary layer, Tu_e. However, the SA turbulence model [9] is used herein, where the Tu_e information is not available. Therefore, utilizing the freestream turbulence intensity Tu_∞ to determine the critical amplification factor is the only option, even though the relation between N_{crit} and Tu_∞ is not truly physics based in the bypass transition regime.

Therefore, in this work, the goal is to focus on calibrating the critical amplification using a gradient-based optimization of the transition onset location in order to resolve the discrepancies between CFD predictions and the experimental data. Ultimately, the calibrated amplification factors for a set of canonical test cases can be used for determining a new relation, similar to Eq. (4). This new relation can be obtained using a polynomial-based regression model and can be tuned for a wide range of transitional boundary layers including both bypass and natural transition processes.

B. Turbulence Model

The AFT model described in this work is developed with the main intention of being used in conjunction with the one-equation turbulence model of Spalart and Allmaras [9]. Therefore, details of the SA turbulence model and its coupling with the AFT transition model are presented in this section.

1. Spalart–Allmaras Model

The SA turbulence model used in this work is defined in its conservative form [32] as

$$\frac{\partial \rho\tilde{\nu}}{\partial t} + \underbrace{\frac{\partial \rho u_j \tilde{\nu}}{\partial x_j}}_{\text{convective flux}} - \underbrace{\frac{1}{\sigma}\left[\frac{\partial}{\partial x_j}(\rho(\nu+\tilde{\nu}))\frac{\partial \tilde{\nu}}{\partial x_j}\right]}_{\text{diffusive flux}} = \underbrace{\rho c_{b1}(1-f_{t2})\tilde{S}\tilde{\nu}}_{\text{production source term}}$$
$$\underbrace{-\rho[c_{w1}f_w - \frac{c_{b1}}{\kappa^2}f_{t2}]\left(\frac{\tilde{\nu}}{d}\right)^2}_{\text{destruction source term}} + \underbrace{\frac{1}{\sigma}\left[\rho c_{b2}\frac{\partial \tilde{\nu}}{\partial x_i}\frac{\partial \tilde{\nu}}{\partial x_i} - (\nu+\tilde{\nu})\frac{\partial \rho}{\partial x_i}\frac{\partial \tilde{\nu}}{\partial x_i}\right]}_{\text{diffusion source term}} \quad (5)$$

where $\tilde{S}$ is the limited magnitude of the strain rate tensor to avoid having it reach zero or to become negative [32]. In the present work and as recommended by Coder [15], the *negative* version of the SA, i.e., SA-neg, is being used. The SA-neg model is identical to the standard model whenever the modified eddy viscosity $\tilde{\nu}$ is greater than or equal to zero. However, for cases where $\tilde{\nu}$ becomes negative, instead of clipping the turbulence model solution, the source terms are slightly varied and the following equation is solved instead:

$$\frac{\partial \rho\tilde{\nu}}{\partial t} + \underbrace{\frac{\partial \rho u_j \tilde{\nu}}{\partial x_j}}_{\text{convective flux}} - \underbrace{\frac{1}{\sigma}\left[\frac{\partial}{\partial x_j}(\rho(\nu+\tilde{\nu}f_n))\frac{\partial \tilde{\nu}}{\partial x_j}\right]}_{\text{diffusive flux}} = \underbrace{\rho c_{b1}(1-c_{t3})\Omega\tilde{\nu}}_{\text{production source term}}$$
$$+ \underbrace{\rho c_{w1}\left(\frac{\tilde{\nu}}{d}\right)^2}_{\text{destruction source term}} + \underbrace{\frac{1}{\sigma}\left[\rho c_{b2}\frac{\partial \tilde{\nu}}{\partial x_i}\frac{\partial \tilde{\nu}}{\partial x_i} - (\nu+\tilde{\nu})\frac{\partial \rho}{\partial x_i}\frac{\partial \tilde{\nu}}{\partial x_i}\right]}_{\text{diffusion source term}} \quad (6)$$

It is important to notice that the sign of the destruction term is positive for the modified equation being solved in the SA-neg model for $\tilde{\nu} < 0$ cases [Eq. (6)], as opposed to the standard model. Moreover, the limited magnitude of the strain rate tensor $\tilde{S}$ is replaced with the vorticity magnitude Ω in the production term of Eq. (6). Additionally, the f_n function used in the diffusive flux is described as

$$f_n = \frac{c_{n1} + \chi^3}{c_{n1} - \chi^3} \quad (7)$$

where $\chi = \tilde{\nu}/\nu$ and $c_{n1} = 16$ [32]. Note that the rest of the closure coefficients and settings are identical to those from the standard model, details of which are provided in Ref. [9].

2. Coupling of Turbulence and Transition Models

As can be seen, the SA-Standard or the SA-neg models described in the previous section utilize a "tripping" function f_{t2} in the definition of their production and destruction source terms. The goal of the f_{t2} function in the SA model, by design, has been to provide a tripping effect at the transition onset as well as a laminarization effect for small $\tilde{\nu}$ solutions. Therefore, the AFT2019 model tries to exploit this built-in functionality by modifying the f_{t2} term to include the solution of the AFT model intermittency equation such that

$$f_{t2} = c_{t3}(1-\gamma) \quad (8)$$

where $c_{t3} = 1.2$ according to the SA model [9,15]. Additionally, the baseline values for the closure coefficients of the standard AFT model are described and presented in Table 1.

Table 1 Baseline closure coefficients used in the AFT transition model [15]

Coefficient	Value
c_1	100.0
c_2	0.06
c_3	50.0
σ_n	1.0
σ_γ	1.0

3. Boundary Conditions and Additional Numerical Considerations

Finally, the transport equations solved for the SA turbulence model as well as the AFT transition model also require a proper boundary condition treatments. In general, the SA model uses a Dirichlet boundary condition at both far-field and wall boundaries where $\tilde{\nu}$ is set to zero at viscous walls, whereas being set according to a user-specified eddy viscosity ratio χ_∞ at inflow and far-field boundaries. For the standard SA model used for fully turbulent test cases, the recommended value of χ_∞ is between 3.0 and 5.0 [9,32]. However, in order to avoid saturating the incoming flow in the transitional cases, a smaller value of 0.1 is recommended for χ_∞ when AFT transition model is being utilized. Moreover, the AFT transition model uses a Dirichlet boundary condition for both $\tilde{n}$ and γ at the inflow and far field with $\tilde{n} = 0.0$ and $\gamma = 1.0$ while using a Neumann condition at outflow and viscous wall boundaries.

Another important aspect in the implementation of the AFT model and its coupling with the underlying SA turbulence model is to address numerical and stability considerations. As such, the local shape factor H_L needs to be limited within $[-0.25, 200]$ for numerical stability. Additionally, the solutions to the amplification factor as well as the intermittency equations must be bounded to avoid spurious or nonphysical solutions appearing in the flowfield. In this work, the value of $\tilde{n}$ is bound within $[-1, 20]$ at the end of each time-step. Similarly, the value of the intermittency γ is bound within $[0, 1]$. In addition to these lower and upper bounds for the AFT model solutions, the maximum change for both $\tilde{n}$ and γ is also limited to 50% relative to their values at the previous step. This residual limiting is found to be essential for promoting a good convergence behavior for the AFT model.

C. Adjoint Method for Sensitivity Analysis and Calibration

Before presenting the design optimization problem, let us first consider a typical minimization problem for an objective function $I(\boldsymbol{x}, \boldsymbol{Q}(\boldsymbol{x}))$, defined as

$$\min_{\boldsymbol{x}} I(\boldsymbol{x}, \boldsymbol{Q}(\boldsymbol{x})) \quad \text{subject to } \boldsymbol{R}(\boldsymbol{x}, \boldsymbol{Q}(\boldsymbol{x})) = 0 \quad (9)$$

where $\boldsymbol{x}$ is the vector of design variables, $\boldsymbol{Q}$ is the vector of flow solutions (conservation variables), and $\boldsymbol{R}$ represents the vector of flow residuals for the primal governing equations. The optimization problem defined here aims at identifying the optimal design, $\boldsymbol{x}_{\text{optimal}}$, that minimizes the objective function subject to a "fully converged" or *feasible*, primal CFD solution, i.e., $\boldsymbol{R}(\boldsymbol{x}, \boldsymbol{Q}(\boldsymbol{x})) = 0$. Using the method of Lagrange multipliers, the minimization problem given in Eq. (9) can be reformulated as a functional such that

$$\mathcal{L}(\boldsymbol{x}, \boldsymbol{Q}, \boldsymbol{\psi}) = I(\boldsymbol{x}, \boldsymbol{Q}(\boldsymbol{x})) + \boldsymbol{\psi}^T \boldsymbol{R}(\boldsymbol{x}, \boldsymbol{Q}(\boldsymbol{x})) \quad (10)$$

where $\boldsymbol{\psi}$ is the vector of adjoint solutions. The next step is to minimize the Lagrangian functional $\mathcal{L}(\boldsymbol{x}, \boldsymbol{Q}, \boldsymbol{\psi})$, which can be accomplished using the Karush–Kuhn–Tucker (KKT) optimality conditions:

$$\frac{\partial \mathcal{L}}{\partial \boldsymbol{\psi}} = \boldsymbol{R}(\boldsymbol{x}, \boldsymbol{Q}(\boldsymbol{x})) = 0 \quad (11)$$

$$\frac{\partial \mathcal{L}}{\partial \boldsymbol{x}} = \frac{\partial I}{\partial \boldsymbol{x}} + \boldsymbol{\psi}^T \frac{\partial \boldsymbol{R}}{\partial \boldsymbol{x}} = 0 \quad (12)$$

$$\frac{\partial \mathcal{L}}{\partial \boldsymbol{Q}} = \frac{\partial I}{\partial \boldsymbol{Q}} + \boldsymbol{\psi}^T \frac{\partial \boldsymbol{R}}{\partial \boldsymbol{Q}} = 0 \quad (13)$$

Here, the first KKT condition is the original primal governing equations presented earlier in Eq. (9). Additionally, the second KKT condition is nothing but the total derivative of the original objective function with respect to the vector of design variables. This can be proven by writing the total derivative or sensitivity as

$$\frac{dI}{dx} = \frac{\partial I}{\partial x} + \frac{\partial I}{\partial Q}\frac{\partial Q}{\partial x} \tag{14}$$

It must be noted that the last term in Eq. (14) is very expensive to calculate. In the discrete adjoint approach, the general assumption is that the governing equations for the primal flow are satisfied, which would require converging the primal CFD solver to machine precision. Therefore, based on the assumption of the converged primal solution, i.e., $\boldsymbol{R}(\boldsymbol{x}, \boldsymbol{Q}(\boldsymbol{x})) = 0$, one can show that

$$\boldsymbol{R} = 0 \rightarrow \frac{d\boldsymbol{R}}{d\boldsymbol{x}} = \frac{\partial \boldsymbol{R}}{\partial \boldsymbol{x}} + \frac{\partial \boldsymbol{R}}{\partial \boldsymbol{Q}}\frac{\partial \boldsymbol{Q}}{\partial \boldsymbol{x}} = 0 \rightarrow \frac{\partial \boldsymbol{Q}}{\partial \boldsymbol{x}} = -\left[\frac{\partial \boldsymbol{R}}{\partial \boldsymbol{Q}}\right]^{-1}\frac{\partial \boldsymbol{R}}{\partial \boldsymbol{x}} \tag{15}$$

which is the cornerstone of the discrete adjoint approach. Here, $\partial \boldsymbol{R}/\partial \boldsymbol{Q}$ is the Jacobian of the primal solver. By rearranging and inserting Eq. (15) into Eq. (14), we can rewrite the total derivative as

$$\frac{dI}{dx} = \frac{\partial I}{\partial x} \underbrace{- \frac{\partial I}{\partial \boldsymbol{Q}}\left[\frac{\partial \boldsymbol{R}}{\partial \boldsymbol{Q}}\right]^{-1}}_{\Lambda}\frac{\partial \boldsymbol{R}}{\partial \boldsymbol{x}} \tag{16}$$

It can be easily shown that the Λ term in Eq. (16) is identical to the transposed adjoint solution vector $\boldsymbol{\psi}^T$ in Eqs. (10–13), such that

$$\frac{\partial \mathcal{L}}{\partial \boldsymbol{Q}} = \frac{\partial I}{\partial \boldsymbol{Q}} + \boldsymbol{\psi}^T\frac{\partial \boldsymbol{R}}{\partial \boldsymbol{Q}} = 0 \rightarrow \boldsymbol{\psi}^T = -\frac{\partial I}{\partial \boldsymbol{Q}}\left[\frac{\partial \boldsymbol{R}}{\partial \boldsymbol{Q}}\right]^{-1} \tag{17}$$

Typically, the inverse of the Jacobian matrix $\partial \boldsymbol{R}/\partial \boldsymbol{Q}$ is not found explicitly. Instead, we solve the corresponding linear system with the appropriate right-hand-side vector by transposing the Jacobian, which yields the *adjoint equations*:

$$\frac{\partial \boldsymbol{R}^T}{\partial \boldsymbol{Q}}\boldsymbol{\psi} = -\frac{\partial I^T}{\partial \boldsymbol{Q}} \tag{18}$$

The above equation is also known as the adjoint flow equation. Next, the calculated adjoint vector is substituted into Eq. (16) to compute the total derivative

$$\frac{dI}{dx} = \frac{\partial I}{\partial x} + \boldsymbol{\psi}^T\frac{\partial \boldsymbol{R}}{\partial \boldsymbol{x}} \tag{19}$$

A very important point to make here is that the design variables $\boldsymbol{x}$ do not appear in Eq. (18). This means that the computational cost of the adjoint method is only proportional to the number of objective functions and is independent of the number of design variables. The quantity of interest or the objective function for the calibration problem studied in this work [presented in Eq. (9)] will be described in the following section.

D. Calibration Based on a Minimization Problem

The main goal of the present work is to calibrate the critical amplification factor via a gradient-based optimization framework. To achieve this goal, experimental data available for various benchmark test cases will be used for an adjoint-based minimization problem where the critical amplification factor N_{crit} is used as the design variable. Here, the optimization problem is set up to minimize the prediction errors defined as the difference between numerical and experimental results in terms of the transition onset location. Therefore, the minimization problem used in this work can be described as

$$\min_{N_{crit}} I = \frac{1}{2}(x_{cr} - x_{cr}^{target})^2 \tag{20}$$

where x_{cr} and x_{cr}^{target} are the critical or the transition onset locations from the numerical and experimental studies, respectively. Similar to an earlier work by the authors [4], the turbulence index proposed by Spalart and Allmaras in their seminal work [9] will be used for an accurate prediction of the transition onset location. This index is defined as

$$i_t = \frac{1}{\kappa u_\tau}\frac{\partial \tilde{\nu}}{\partial n} \tag{21}$$

where wall shear velocity u_τ is approximated as $u_\tau \approx \sqrt{\nu\Omega}$, and n is the wall-normal direction. The turbulence index described in Eq. (21) will have a value close to zero in laminar regions while switching rapidly to a value close to one in turbulent regions. According to Spalart and Allmaras [9], the value of i_t can rise slightly above one in the turbulent boundary layer as it approaches separation. The goal here is to utilize this turbulence index as measure to determine the onset or critical location x_{cr} that can be used in the definition of the quantity of interest described in Eq. (20). For the purpose of the gradient-based calibration, it is essential to have a differentiable path between the objective function and the set of design variables as well as the flow solution. Therefore, a nonlinear least-squares minimization problem is used to fit a sigmoid function to the turbulence index profile. The process is shown in Fig. 1 for a typical turbulence index profile where the transition onset location is determined based on the location at which the turbulence index reaches a value of $i_t = 0.5$.

It must be noted that another choice for the objective function in these types of calibration problems would be the L2-error of the skin friction profiles between the CFD solver and the experimental measurements. However, the skin friction data for most experimental studies do not cover the entire span of the viscous wall, which can create discontinuities in the objective function. Therefore, as will be shown later in this work, the choice of the turbulence index profile with the sigmoid fit used for determining the onset location is a viable option that also leads to a smooth and continuous design space. Note that gradient-based optimization is prone to getting trapped in local optima. However, the calibration sought in this work is based on an objective function that approaches zero when the target transition onset location is reached. Therefore, it is hypothesized that such behavior proves the well-posedness of the design space that can guarantee the optimizer would converge to the sought optimum. Finally, the calibration or the minimization problem is solved using the in-house Unstructured Parallel Compressible Design Optimization Framework (UNPAC-DOF) [33,34].

III. Calibration of the Critical Amplification Factor

As was shown in an earlier work [4], achieving a universal set of optimal closure coefficients that result in improved predictions for a range of benchmark test cases would be improbable if not impossible. Additionally, due to the flipped signs of sensitivities for the main closure coefficients of the AFT transition model, a multipoint optimization of the coefficients would be ill-posed. As such, the attention is focused on the calibration of the critical amplification factor for canonical flat-plate test cases (both bypass and natural transition) in order to define a newly calibrated relation that could potentially be

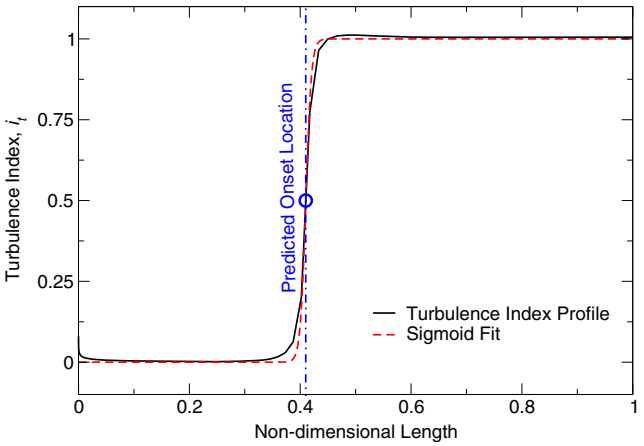

Fig. 1 Turbulence index profile and the fitted sigmoid function based on a nonlinear least-squares minimization. Notice the transition onset location predicted at $i_t = 0.5$, which also happens to be where the value of the sigmoid function reaches 0.5.

used in place of the Mack's relation. As discussed earlier, the AFT model is based on the linear instability growth that is mainly relevant for FSTI values less than 1%. However, from the model development standpoint, including both bypass and natural transition test cases in our calibration process offers continuity between both transitional flow regimes. Therefore, the goal of this study is to use gradient-based optimization to calibrate the critical amplification factor so as to match experimentally reported transition onset location. For this purpose, four canonical test cases are chosen, which will be described next. Once the calibrated critical amplification factors are determined, those are used to relate them to experimentally reported FSTI values, which is similar to Mack's original relation.

A. Canonical Flat Plate Test Cases

Four canonical test cases used for N_{crit} calibration involve zero pressure gradient flow around flat plates. The flow conditions as well as the approximate transition onset locations from the experimental data are reported in Table 2. The first two test cases (T3A and T3B) involve a relatively low Reynolds number and a high freestream turbulence intensity, which results in the bypass transition through a secondary instability mode. It must be noted that the AFT model, which relies on the linear stability theory, is better suited for natural transition associated with relatively lower values of freestream turbulence intensity. Therefore, two natural transitional cases are also chosen for this study, which involve a relatively low freestream turbulence intensity and a higher Reynolds number. The first natural transitional case is selected from the ERCOFTAC T3 series [35] and is known as the T3A- (also referred to as T3AM). The classical benchmark case of Schubauer and Klebanoff (S&K) is also considered in this work, which involves the natural transition of the boundary layer as a result of very low freestream turbulence intensity.

Table 2 Freestream flow conditions for the canonical test cases used for the sensitivity analysis

Case	Re_L	FSTI ($Tu\%$)	Re_c	$x_{\text{cr}}^{\text{target}}/L$	Transition type
T3A	360,000	3.0	198,000	0.55	Bypass
T3B	630,000	6.0	63,000	0.10	Bypass
T3A-	1,320,000	0.9	1,914,000	1.45	Natural
S&K	3,400,000	0.03	3,060,000	0.90	Natural

Table 3 Model parameters gathered from various numerical studies for the S&K natural transitional flat plate test case (FSTI = 0.03%) [36]

FSTI ($Tu\%$)	N_{crit}	References
0.03	11.04	[6,11,47]
0.041	**10.3**	[15]
0.07	**9.0**	[28,37]
0.1	8.15	[10]
0.18	6.74	[5,7,38]

As discussed earlier, a common practice in the CFD community is to manually tune the model parameters, i.e., either the FSTI or the critical amplification factor, for each individual case. An example of this approach can be seen in the model parameter data gathered from the literature for the S&K [36] benchmark study. The experimentally measured and reported FSTI for this case is 0.03%, and different model parameters used in various numerical studies (the actual prescribed model parameters are in bold next to their corresponding N_{crit} or FSTI value calculated using the Mack's relation or its inverse, respectively) are presented in Table 3.

As seen from Table 3, a majority of modeling efforts modify the freestream turbulence intensity, which sets the critical amplification factor through Mack's relation, from its experimentally calculated value in order to reduce the discrepancies between CFD and experimental results [2,5,7,10,11,14,15,28,38].

Additionally, the target transition onset locations for these cases are also provided in Table 2 in terms of the reference length L based on the critical Reynolds number determined from the experimental data. For the calibration of the critical amplification factor, these target transition onset locations are used in the objective function of Eq. (20). The objective function is then minimized using the smooth version of the SA-AFT2019 model described earlier in this work. Here, a bound-constrained optimization is adopted with the lower and upper bounds for the design variable, i.e., the critical amplification factor, set to 0.01 and 12.0, respectively. The calibration results are shown in Figs. 2 and 3 for the bypass and natural transitional cases in terms of skin friction coefficient profiles. It is seen that the agreements between our predictions and the experimental data are significantly improved with all four cases ultimately calibrating the critical amplification factor to an optimal value that results in the correct prediction of the onset location (according to the experimental data).

Calibrated values of the critical amplification factor for the four test cases are summarized in Table 4. Also presented are the corresponding freestream turbulence intensities for the calibrated N_{crit} value based on the inverse of the Mack's relation [Eq. (4)] It must be noted that the Mack's relation augmented with the Drela's hyperbolic tangent limiter is bounded to small but positive values of the critical factor for large turbulence intensities. Therefore, the calibrated N_{crit} value of 0.116 for the T3B case is in fact unattainable with the limited form of Mack's original relation. However, as was seen in Fig. 2, when the solver is run with the calibrated value of the critical amplification factor, a significant improvement in the prediction of the onset location is achieved using the in-house CFD solver.

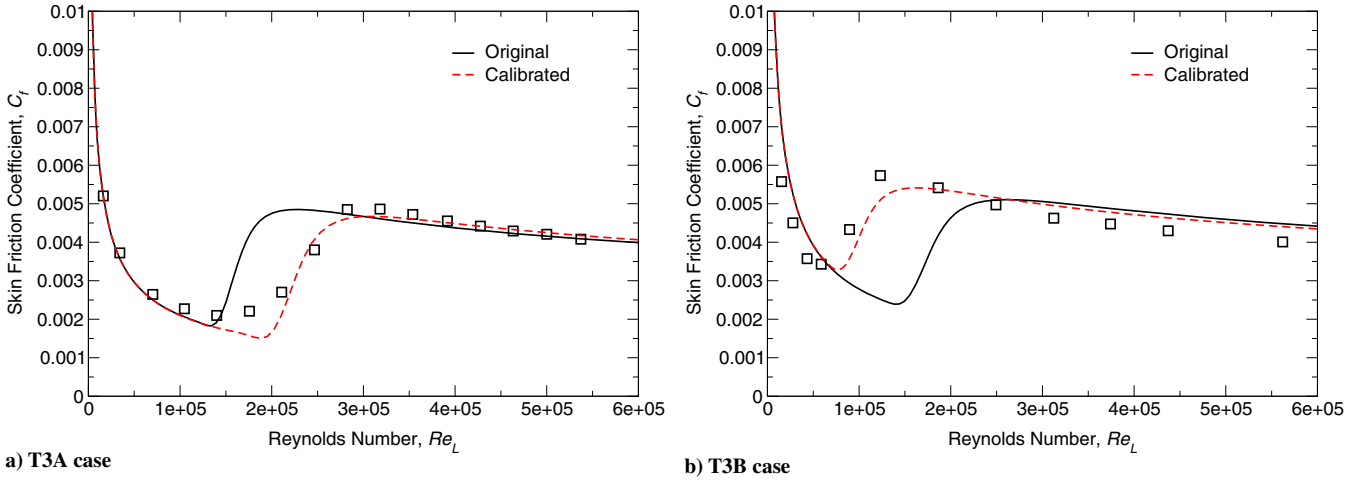

a) T3A case b) T3B case

Fig. 2 Comparison of the skin friction coefficient profiles obtained using the original and calibrated N_{crit} for the bypass transitional cases with experimental data from Ref. [35].

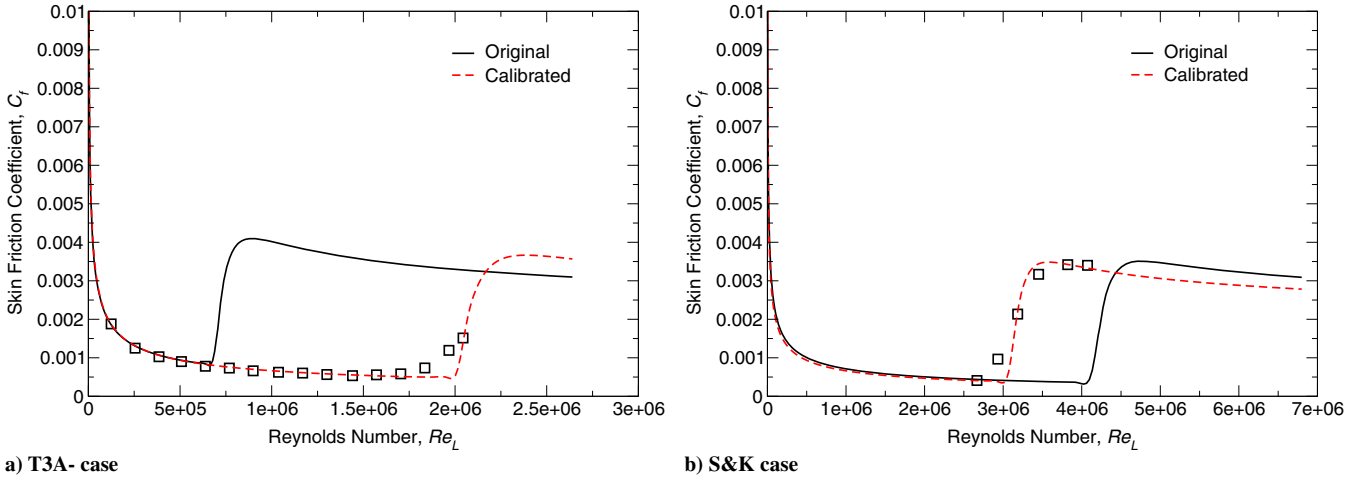

Fig. 3 Comparison of the skin friction coefficient profiles obtained using the original and calibrated N_{crit} for the natural transitional cases with experimental data from Refs. [35,36].

Table 4 Original and calibrated critical amplification factors for the canonical flat plate test cases

Case name	FSTI (Tu%)	N_{crit} [Mack, Eq. (4)]	N_{crit} (calibrated)	FSTI (inverse Mack)
T3A	3.0	0.86	1.212	2.268%
T3B	6.0	0.463	0.116	N/A
T3A-	0.9	2.976	5.930	0.253%
S&K	0.03	11.04	7.703	0.1205%

B. Calibrated Relation for Turbulence Intensity Versus Critical Amplification Factor

With the calibrated values of the critical amplification factor we can now focus on a regression model that can serve as a calibrated relation for determining N_{crit} as a function of the freestream turbulence intensity that can be used in lieu of Mack's relation. First, the calibrated critical factors for the bypass and natural transitional cases are plotted against the Mack's relation and the results are shown in Fig. 4. Also shown are some of the critical amplification factors that are chosen in the CFD community for improving the transition predictions for these standard test cases. It must be noted that in some of these studies, the authors have simply chosen a different FSTI compared to the reported values from the experimental data. In such cases, the corresponding N_{crit} value obtained from Eq. (4) is shown. Additionally, in studies involving linear stability and e^N models for transition prediction, the actual value of the N_{crit} is shown. It is important to note that our calibrated critical amplification factors are in line with the typical values used in the CFD community except for the T3A- case, where the critical factor is pushed to a significantly higher value. However, to the best of the authors' knowledge, this is the first work reported in the literature that utilizes a gradient-based optimization technique for determining the optimal critical amplification factor in order to calibrate the transition onset location predictions.

Before fitting a regression model to the calibrated critical factors, it is important to note that our calibrated N_{crit} factors for the natural transitional cases, i.e., S&K and T3A-, show the largest discrepancies with the original values obtained from the Mack's relation. Therefore, a weighted averaging has been utilized to alleviate these discrepancies that could be associated, to some extent, with the challenging nature of these low freestream turbulence intensity cases. Finally, a fourth-order polynomial regression model is used and the coefficients are obtained using a least-squares optimization method. Additionally, a modification similar to that suggested by Drela [12] is utilized to avoid negative values of the critical amplification factor with a limit of 2.5% as suggested by Coder [15]. The calibrated relation is described as

$$N_{crit} = a_0 + a_1\tau + a_2\tau^2 + a_3\tau^3 + a_4\tau^4 \quad \tau = 2.5\tanh\left(\frac{Tu\%}{2.5}\right) \tag{22}$$

where the coefficients a_0 through a_4 are described in Table 5. It is important to note that the calibrated relation preserves positive values of N_{crit} for a maximum FSTI value of around 10%.

Finally, the new regression model is plotted against Mack's original relation and the results are shown in Fig. 5. As can be seen, the calibrated relation agrees well with the critical factor values used by the CFD community although ours is based on a gradient-based calibration process. Additionally, it is important to notice the exact

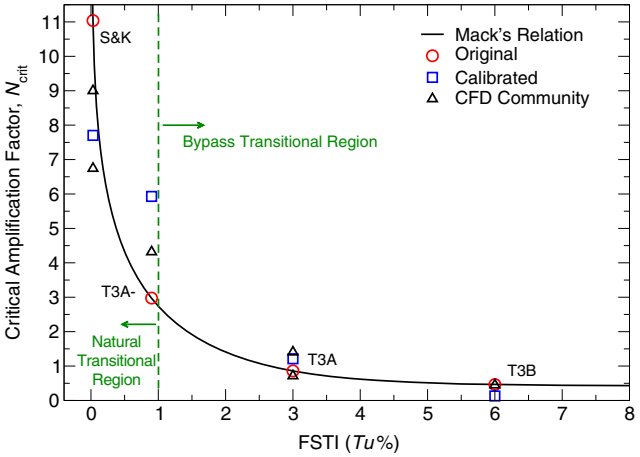

Fig. 4 Comparison of the original critical factors N_{crit} from the Mack's relation [Eq. (4)] and the calibrated values for the canonical flat plate cases. Also shown are typical N_{crit} values used in the CFD community [7,10,11].

Table 5 Coefficients of the calibrated relation for obtaining the critical amplification factor N_{crit} as a function of the freestream turbulence intensity

Coefficient	Value
a_0	9.0064
a_1	−4.4958
a_2	−1.4208
a_3	1.5920
a_4	−0.3532

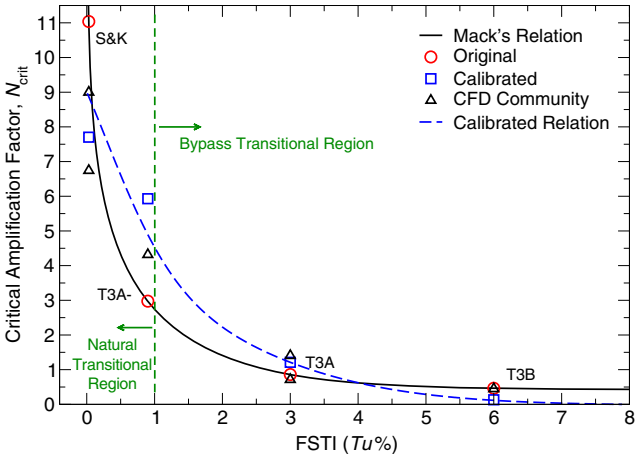

Fig. 5 Comparison of our newly calibrated relation for obtaining the critical amplification factor N_{crit} as a function of the freestream turbulence intensity to the original Mack's relation [Eq. (4)].

fitting of the calibrated factors in the bypass region as opposed to the approximate fitting of the calibrated factors in the natural transitional region. In fact, the use of the weighted averaging for the natural transitional region puts our calibrated relation more in-line with the critical factors used in other studies reported in the literature.

IV. Validation and Verification of the Calibrated Critical Amplification Factors

To verify the efficacy of the newly calibrated relation for the critical amplification factor, the natural transitional flows past the NLF(1)-0416 and the S809 airfoils are studied. The goal here is to study the effects of the calibrated critical amplification factors on RANS-based transition predictions using the AFT2019 model [15,39].

A. Natural Laminar Flow NLF(1)-0416 Airfoil

The NLF(1)-0416 airfoil was designed with the goal of producing a target maximum lift coefficient that would be roughness independent while still having a low profile-drag coefficient similar to what is normally achieved with the NACA 6-series airfoils. Additionally, this airfoil is designed to have long runs of laminar flow resulting from favorable pressure gradients along its surface to attain natural laminar flow [28]. The NLF(1)-0416 test case that will be studied in this work for the purpose of validation and verification (V&V) is subject to a Reynolds number of 4.0 million and a Mach number of 0.1. The freestream turbulence intensity is set to $Tu = 0.045\%$ according to the experimental studies conducted in the NASA Langley Low-Turbulence Pressure Tunnel (LTPT) [40]. It must be noted that this freestream turbulence intensity is also representative of some other low-turbulence wind tunnels such as the Penn State University Low-Speed, Low-Turbulence Wind Tunnel (LSLTT) [41,42] and the Delft University Low-Speed Wind Tunnel (LSWT) [43], which are all designed for very high critical amplification factors [28].

1. Grid Convergence Study

To ensure that the numerical results are grid converged, four different grid resolutions are considered and the grid convergence studies are conducted. These C-typed structured computational grids are provided by the AIAA Transition Modeling and Prediction Workshop (case 2) and are extended to 1000-chord units away from the airfoil based on the recommendation of the workshop organizing committee and in order to reduce any effects on the surface-integrated drag coefficients in the absence of a far-field vortex correction [44]. The four grid resolutions (levels L0–L3) are shown in Fig. 6, where the number of grid nodes around the circumference of the airfoil varies from 512 for the "Medium" (L3) grid to 1536 for the "Ultra Fine" (L0) grid. The minimum wall spacing for the Medium (L3) grid is 3.5×10^{-6} chord length, and the Ultra Fine (L0) grid has a total of 610,657 nodes (see Ref. [13] for more details).

For the purpose of grid convergence study, the freestream flow at a zero-degree angle of attack (AoA) with a freestream turbulence intensity of 0.045% is considered, and the resulting skin friction profiles are presented in Fig. 7 for the finest grid levels, i.e., L0–L2. In general, skin friction profiles are similar for the majority of the surface points with distinct differences in the vicinity of the transition onset location. Furthermore, predicted lift and drag coefficients for different grid resolutions are given in Fig. 8. It is important to note that both the lift coefficient and the drag count settle as the grid resolution is increased. Additionally, the results of the grid convergence study are presented in Table 6, which also includes the differences (in percent) compared to the results obtained on the finest grid, i.e., the Ultra Fine (L0). It can be clearly seen that the differences between the L1 and L0 grids in terms of lift and drag coefficients are small. Therefore, the L1 grid is ultimately chosen for the rest of the results presented in this section.

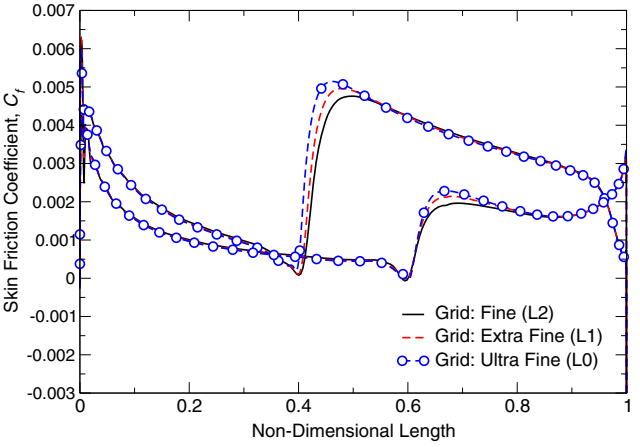

Fig. 7 Grid convergence study in terms of skin friction coefficient for the transitional flow past the NLF(1)-0416 airfoil at 0 deg angle of attack.

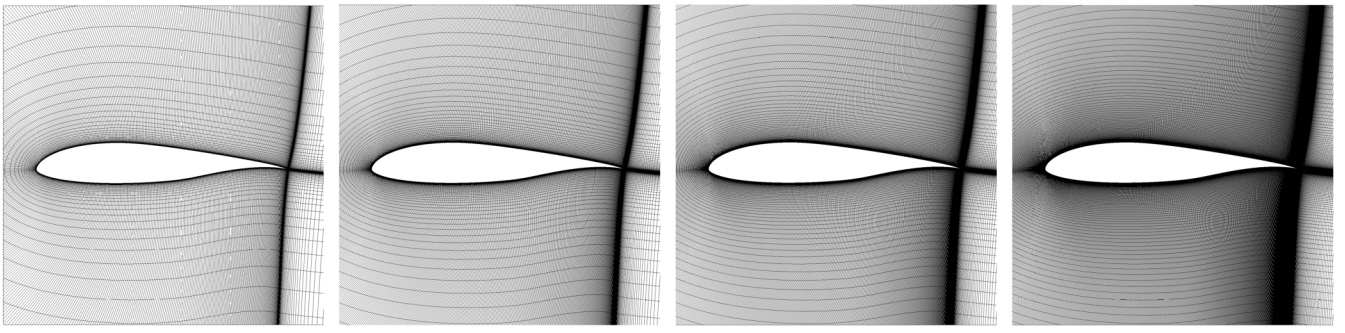

a) L3 grid **b) L2 grid** **c) L1 grid** **d) L0 grid**

Fig. 6 Computational grids for the transitional flow past the NLF(1)-0416 airfoil.

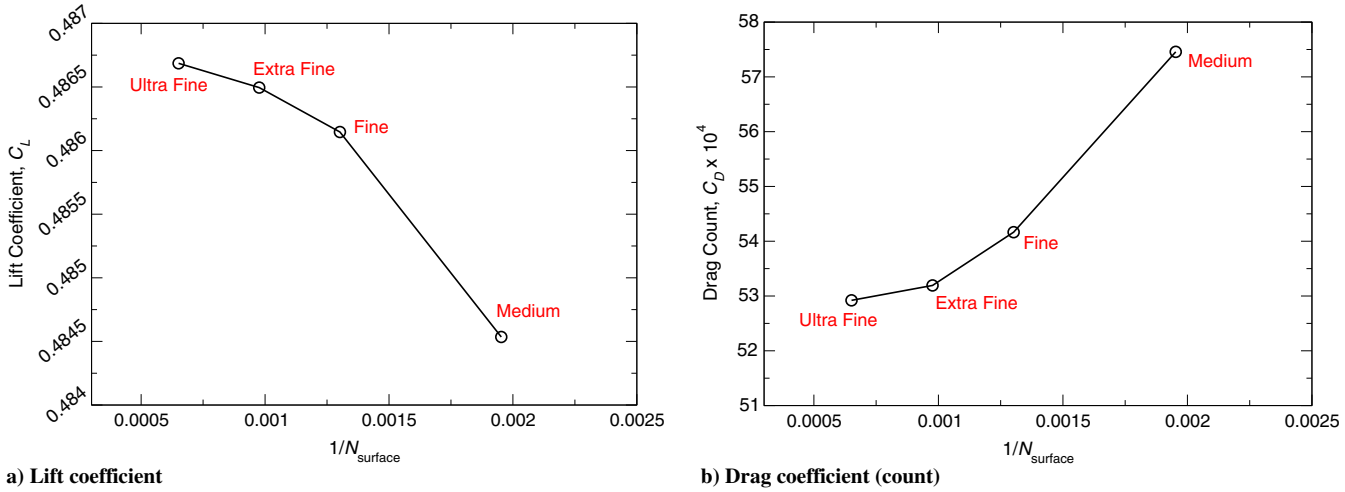

a) Lift coefficient b) Drag coefficient (count)

Fig. 8 Grid convergence study in terms of lift coefficient and drag count for the transitional flow past the NLF(1)-0416 airfoil at 0 deg angle of attack.

Table 6 Results of the grid convergence study in terms of lift coefficient and drag count for the transitional flow past the NLF(1)-0416 airfoil at 0 deg angle of attack

Grid	N_{surf}	$1/N_{surf}$	C_L	Diff. (%)	$C_D \times 10^4$	Diff. (%)
Medium (L3)	512	0.00195	0.484535	0.44	57.457	8.57
Fine (L2)	768	0.00130	0.486146	0.11	54.165	2.35
Extra Fine (L1)	1024	0.00097	0.486495	0.04	53.193	0.51
Ultra Fine (L0)	1536	0.00065	0.486686	— —	52.921	— —

2. *Lift, Drag, and Transition Predictions*

As reported earlier, the value of the freestream turbulence intensity for this case is 0.045% according to the experimental data. However, in many studies available in the literature, the value of the FSTI is increased to 0.15% since the transition onset locations are consistently predicted further downstream of those reported by the experiment [19,29]. This was first reported by Coder [28] and resulted in a significant improvement of the transition predictions compared to the experimental data for the NLF(1)-0416 airfoil in a wide range of angles of attack. It must be noted that the FSTI of 0.045% corresponds to a critical amplification factor of $N_{crit} = 10.07$ according to the Mack's relation [Eq. (4)]. Therefore, by increasing the value of FSTI, the critical amplification factor is in fact reduced to $N_{crit} = 7.18$ [equivalent to $Tu = 0.15\%$ according to Eq. (4)] [28].

In this work, however, the goal is to use the newly calibrated relation instead of the Mack's relation while still using the experimental value of the freestream turbulence intensity, i.e., $Tu = 0.045\%$. This value of FSTI is equivalent to a critical amplification factor of $N_{crit} = 8.8$ according to our new relation [Eq. (22)]. The drag polar for the NLF(1)-0416 airfoil at $Re = 4 \times 10^6$ and $M = 0.1$ for an AoA sweep between $[-8, 8]$ deg is provided in Fig. 9. In general, although the SA-AFT transitional results increase the accuracy of the lift and drag predictions compared to the fully turbulent solutions (obtained via SA-neg model), the agreements with the experimental data are further improved based on the calibrated relation. This finding is not surprising since the critical amplification factor is smaller compared to Mack's original relation. Overall, the flow transitions earlier, resulting in the slight increase in the friction drag coefficients.

Additionally, the transition onset locations on the suction and pressure surfaces are predicted according to the turbulence index profile and the results are presented in Fig. 10. Here, the horizontal error bars represent the likely transition intervals for each lift coefficient data point according to the experimental study results [40]. It is apparent that the transition predictions using the newly calibrated

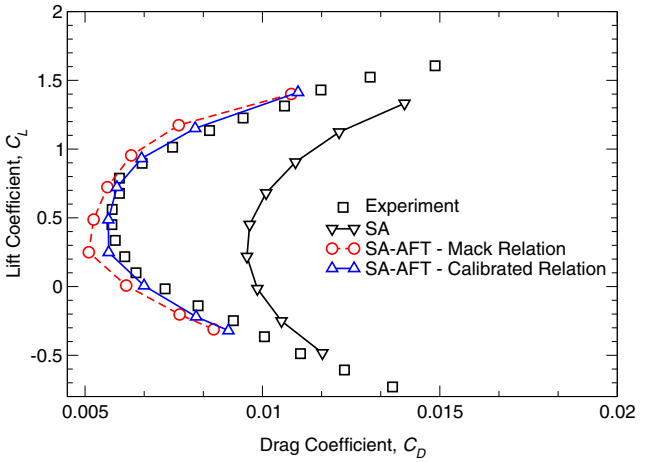

Fig. 9 Drag polar for angles of attack from −8 to 8 deg for the turbulent (SA) and transitional (SA-AFT) cases using the original Mack's and the newly calibrated relations: NLF(1)-0416 airfoil at $Re = 4.0 \times 10^6$, $M_\infty = 0.1$, and $Tu = 0.045\%$. Experimental data are obtained from Ref. [40].

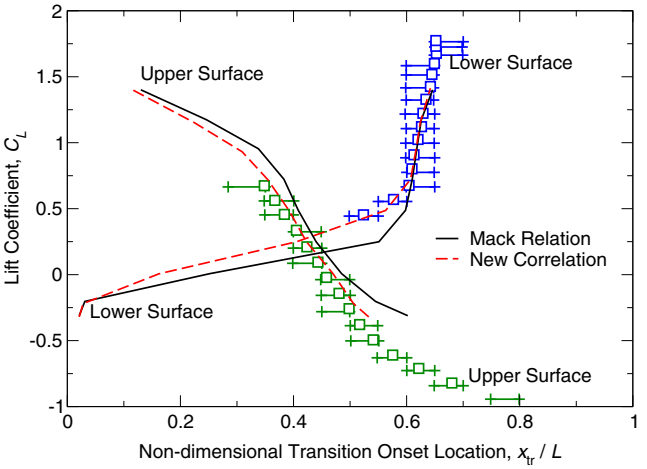

Fig. 10 Transition onset predictions on the top and bottom surfaces of the NLF(1)-0416 airfoil for the transitional (SA-AFT) simulations using the original Mack's and the newly calibrated relations: at $Re = 4.0 \times 10^6$, $M_\infty = 0.1$, and $Tu = 0.045\%$. Experimental data (represented with square symbols) is obtained from Ref. [28].

value of the critical amplification factor agree much better with the experiments compared to those obtained from the Mack's relation. Once again, this result was expected since the reduction of the critical amplification factor according to the newly calibrated relation would lead to the transition onset points consistently shifting toward the leading edge of the airfoil.

Finally, the flow solutions for various angles of attack in terms of Mach number and intermittency are shown in Figs. 11 and 12, respectively. Additionally, the eddy viscosity ratio, μ_t/μ, solutions are presented for the zero AoA case with fully turbulent (SA) and transitional (SA-AFT2019) assumptions based on the newly calibrated value of the $N_{\text{crit}} = 8.8$ and the results are shown in Fig. 13. As can be seen, turbulence in the boundary layer of the NLF(1)-0416 is remarkably overpredicted with the fully turbulent assumption, while the maximum eddy viscosity ratio is almost halved in the transitional flow obtained using the SA-AFT2019 model.

B. S809 Wind Turbine Airfoil

The second validation test case in the natural transitional regime is the S809 airfoil, designed in the 1980s by Dan Somers [45] for stall-regulated wind turbines. This airfoil was also subsequently tested in the TU Delft low-speed and low-turbulence wind tunnel with the turbulence intensity varying from 0.02 to 0.04% for a range of low-speed flow studies [45]. The S809 airfoil has become a standard test case for validation and verification of transition models [13] due to the availability of relatively high-quality wind tunnel measurements and has also been widely used for wind turbine applications [5,46,47]. However, the S809 airfoil exhibits a "drag bucket" on its drag polar, which indicates a rapid change in transition onset location with small AoA variations. This phenomenon causes a sharp increase in the drag coefficient at the edges of the drag bucket where the airfoil maintains a low drag over a range of lift coefficients. Moreover, the experimental measurements of the surface pressure coefficient show a short but intense laminar separation bubble on upper and lower surfaces of the airfoil in the drag bucket region [13]. The specific conditions of interest for this airfoil are $M = 0.1$ and $Re = 2 \times 10^6$ with a freestream turbulence intensity of 0.03%, which is the average turbulence intensity reported for the low-turbulence wind tunnel in Ref. [45].

1. *Grid Convergence Study*

The aforementioned laminar separation bubble and its proper resolution can significantly affect the RANS-based transition modeling, which is why a suitable grid resolution is necessary for an accurate transition prediction. To make sure that the numerical results are grid converged, three different grid resolutions are considered. These C-type structured computational grids are generated according to Ref. [13] and are extended to 1000-chord units away from the airfoil based on the recommendation of the AIAA Transition Modeling and Prediction Workshop organizing committee. The three grid resolutions (levels L0–L2) are shown in Fig. 14, where the number of grid nodes around the circumference of the airfoil varies from 512 for the Fine (L2) grid to 1536 for the Ultra Fine (L0) grid. The minimum wall spacing for the Medium (L3) grid is 6.5×10^{-6} chord-length, and the Ultra Fine (L0) grid has a total of 610,657 nodes (see Ref. [13] for more details).

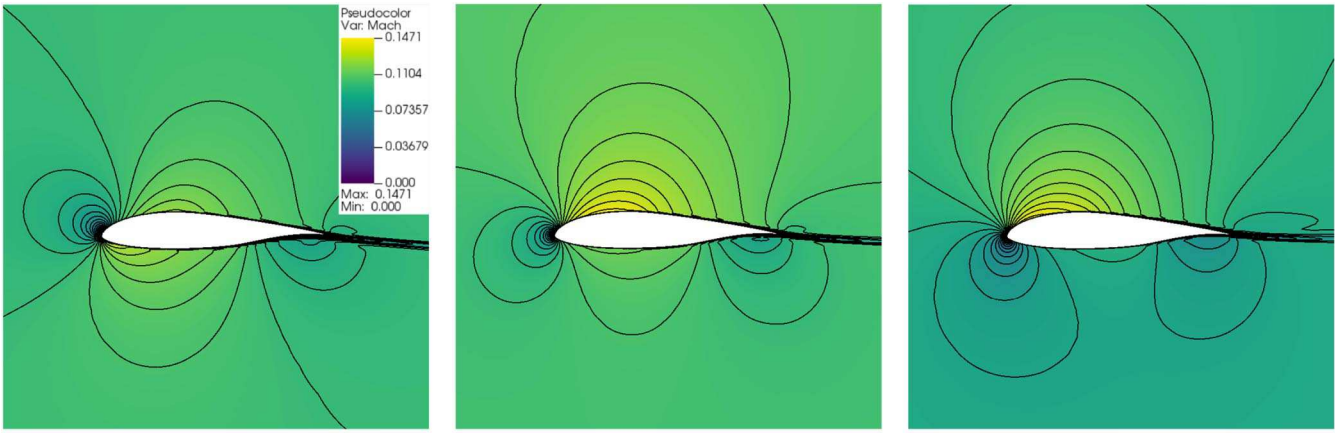

a) AoA = -4 deg b) AoA = 0 deg c) AoA = +4 deg

Fig. 11 Contours of Mach number for transitional flow around NLF(1)-0416 airfoil at various angles of attack, $Re = 4.0 \times 10^6$, $M_\infty = 0.1$, and $Tu = 0.045\%$, using the newly calibrated relation (all plots have same contour levels).

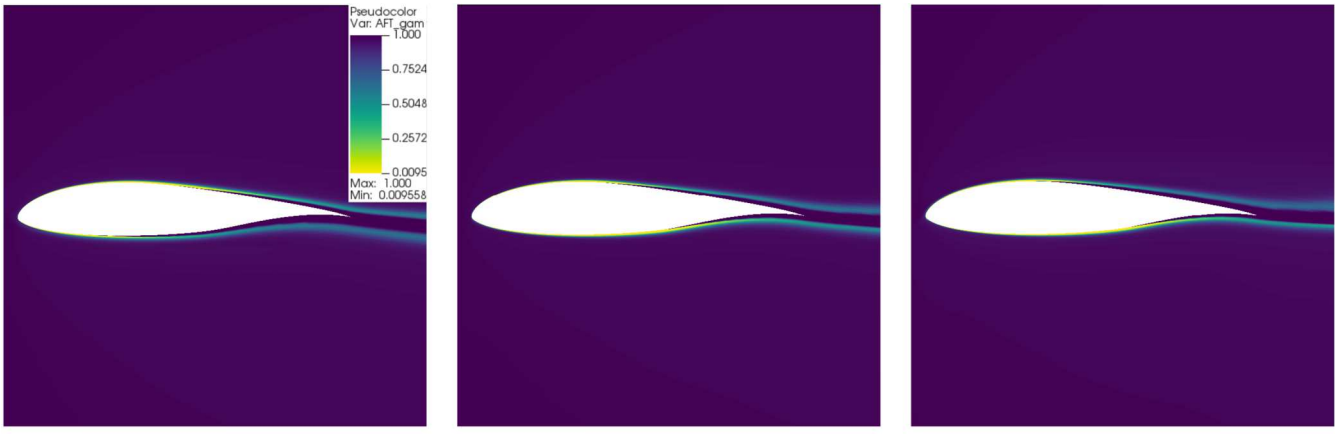

a) AoA = -4 deg b) AoA = 0 deg c) AoA = +4 deg

Fig. 12 Contours of intermittency γ for transitional flow around NLF(1)-0416 airfoil at various angles of attack, $Re = 4.0 \times 10^6$, $M = 0.1$, and $Tu = 0.045\%$, using the newly calibrated relation.

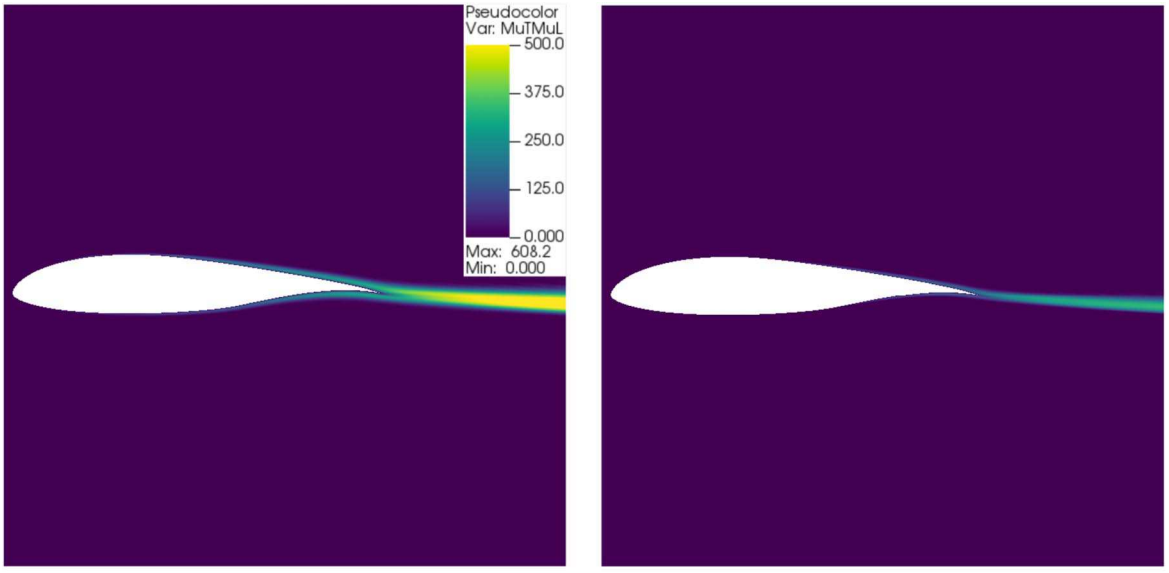

a) Turbulent flow b) Transitional flow

Fig. 13 Contours of eddy viscosity ratio, μ_t/μ_l, for turbulent and transitional flows around NLF(1)-0416 airfoil at 0 deg angle of attack, $Re = 4.0 \times 10^6$, $M_\infty = 0.1$, and $Tu = 0.045\%$, using the newly calibrated relation.

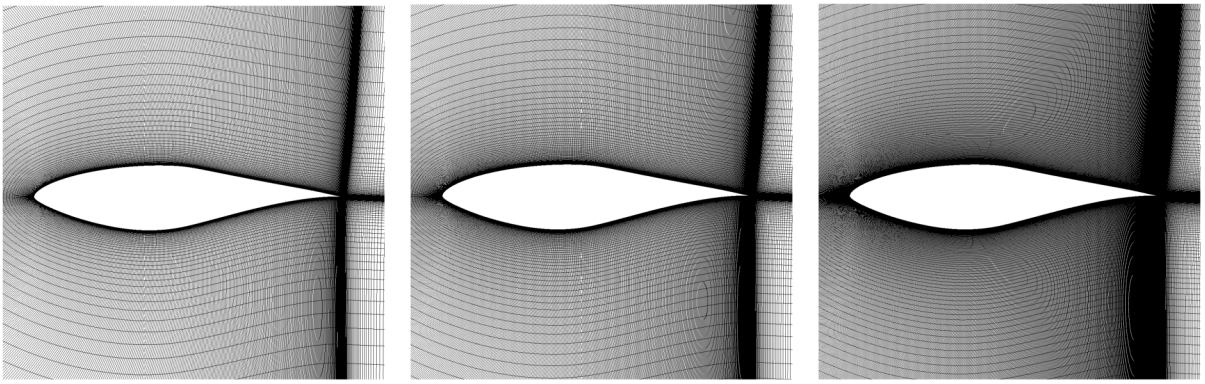

a) L2 (fine) grid b) L1 (extra fine) grid c) L0 (ultra fine) grid

Fig. 14 Computational grids for the transitional flow past the S809 airfoil.

For the purpose of grid convergence study, the freestream flows for angles of attack of 1 and 5 deg with a freestream turbulence intensity of 0.03% are considered, and the results in terms of the surface pressure coefficient are presented in Fig. 15 for three grid resolutions. It is seen that the surface pressure profiles are similar with distinct differences in the vicinity of the transition onset location and the laminar separation bubbles that form on both upper and lower surfaces of the airfoil.

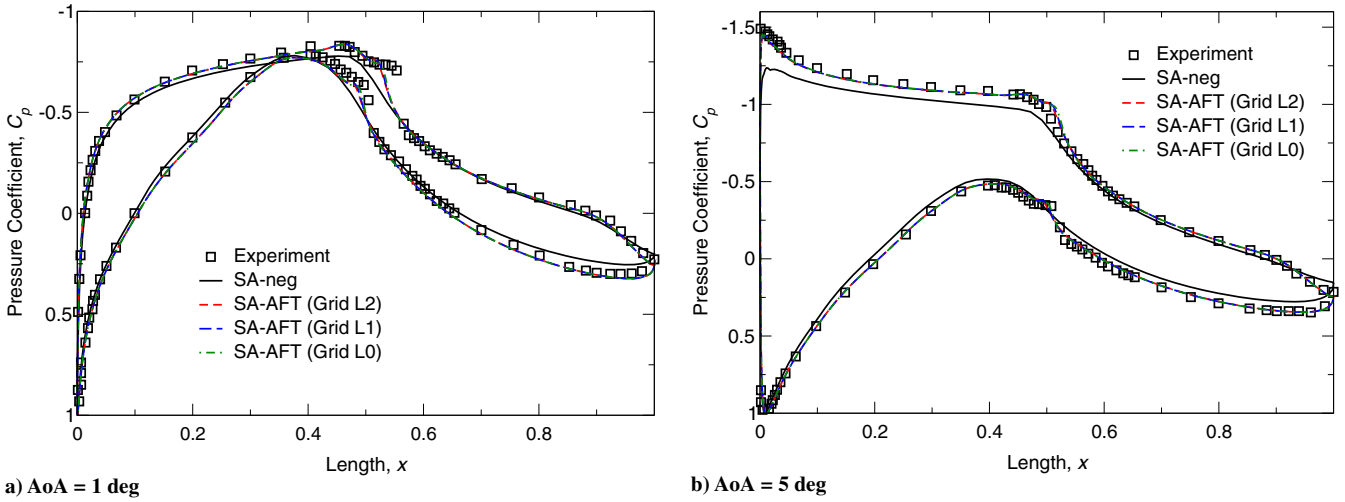

a) AoA = 1 deg b) AoA = 5 deg

Fig. 15 Grid convergence study in terms of surface pressure coefficient for the transitional flow past the S809 airfoil at two different angles of attack.

Note that the experimental results in terms of pressure coefficient distributions [45] that are used herein for comparison are in fact obtained at angles of attack of 1.02 and 5.13 deg, respectively. Additionally, it must be noted that the transitional results agree much better with the experimental profiles than the fully turbulent solutions especially in the aft portion on the pressure side. This is more pronounced in the laminar separation bubbles since this phenomenon is entirely absent in fully turbulent simulations. However, it is interesting to note that the transitional results exhibit a faster transition onset following the formation of the laminar separation bubble, which was also seen in previous works using the AFT2019 model [15].

Additionally, the convergence of the lift and drag coefficients with respect to the grid resolution is studied, and the results are shown in Figs. 16 and 17. It is important to note that both the lift coefficient and the drag count become grid-converged as the resolution is increased. Furthermore, the results of this study are presented in Tables 7 and 8 with the percent differences compared to the finest grid, i.e., the Ultra Fine (L0), level results. As can be clearly seen, the differences between the L1 and L0 grids in terms of lift and drag coefficients are small, which is why the L1 grid is ultimately chosen for the rest of the results presented in this section.

Table 7 Results of the grid convergence study in terms of lift coefficient and drag count for the transitional flow past the S809 airfoil at AoA = 1 deg

Grid	N_{surf}	$1/N_{surf}$	C_L	Diff. (%)	C_D (count)	Diff. (%)
Fine (L2)	768	0.00130	0.284890	0.33	63.524	2.21
Extra Fine (L1)	1024	0.00097	0.285429	0.14	62.583	0.70
Ultra Fine (L0)	1536	0.00065	0.285841	— —	62.145	— —

Table 8 Results of the grid convergence study in terms of lift coefficient and drag count for the transitional flow past the S809 airfoil at AoA = 5 deg

Grid	N_{surf}	$1/N_{surf}$	C_L	Diff. (%)	C_D (count)	Diff. (%)
Fine (L2)	768	0.00130	0.765361	0.35	66.429	3.32
Extra Fine (L1)	1024	0.00097	0.766991	0.14	64.247	0.06
Ultra Fine (L0)	1536	0.00065	0.768086	— —	64.290	— —

2. *Lift, Drag, and Transition Predictions*

The S809 airfoil cases studied in this section are for a Reynolds number of 2 million at a very low freestream turbulence intensity that is typically seen in natural transitional regimes. For these conditions, the S809 airfoil exhibits a significant laminar bucket with very sharp upper and lower boundaries for the lift coefficient. This behavior can be associated with the laminar separation bubble that can effectively fix the transition across a wide range of lift coefficients. As discussed earlier, the value of the freestream turbulence intensity for this case is

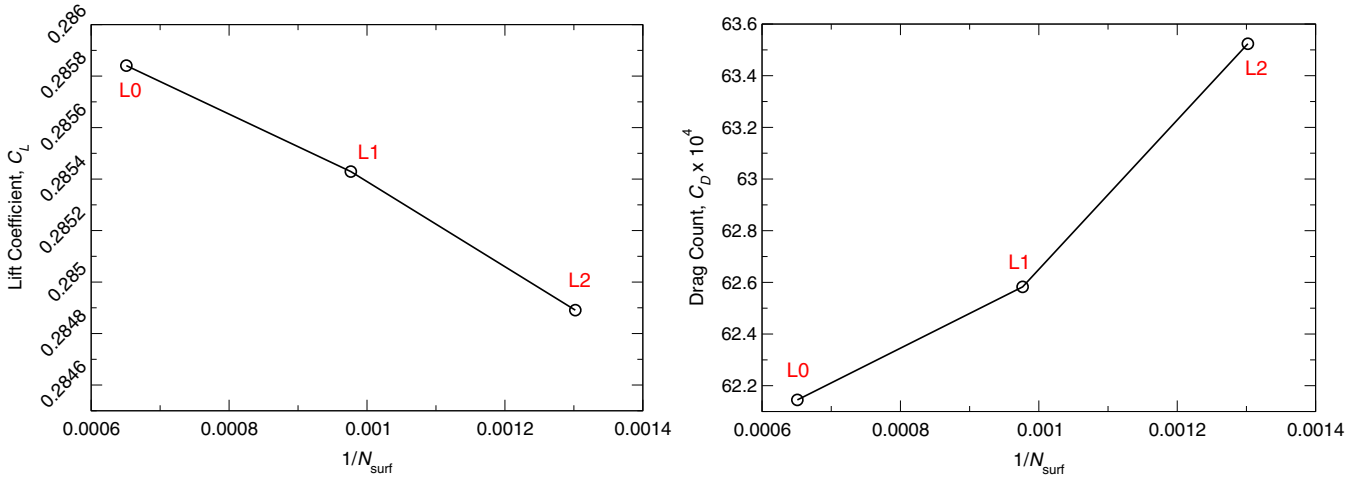

a) Lift coefficient **b) Drag coefficient (count)**

Fig. 16 Grid convergence study in terms of lift coefficient and drag count for the transitional flow past the S809 airfoil at AoA = 1 deg.

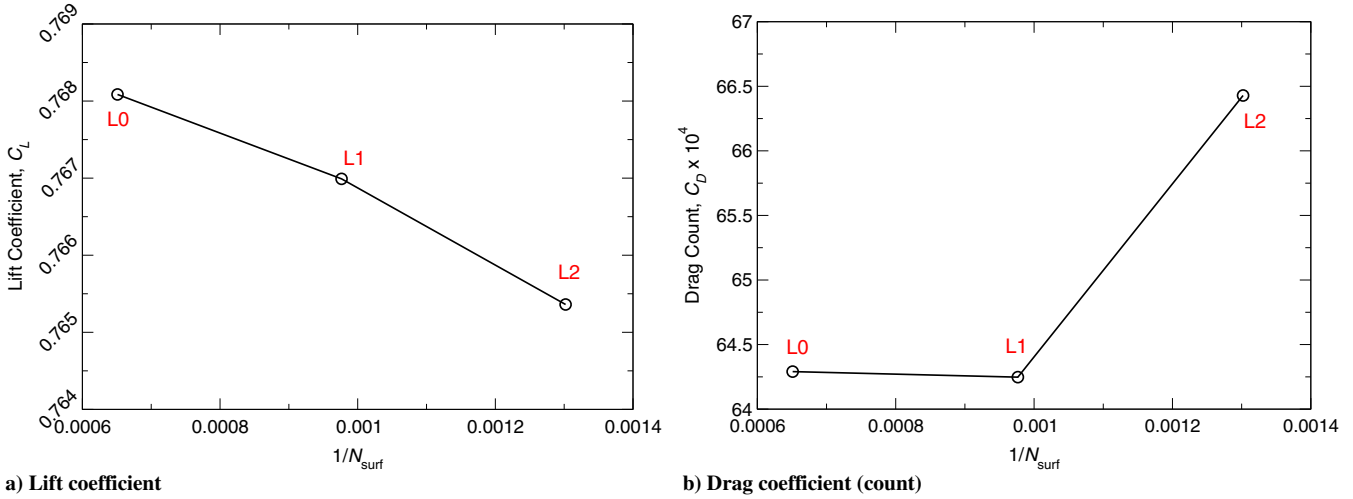

a) Lift coefficient **b) Drag coefficient (count)**

Fig. 17 Grid convergence study in terms of lift coefficient and drag count for the transitional flow past the S809 airfoil at AoA = 5 deg.

$Tu = 0.03\%$ according to the experimental data. This freestream turbulence intensity corresponds to a critical amplification factor of $N_{crit} = 11.04$ according to the Mack's relation [Eq. (4)]. However, this value is recommended to be taken as $N_{crit} = 9.0$ [equivalent to $Tu = 0.07\%$ according to Eq. (4)] [13,15] because a higher FSTI helps alleviating the underprediction of the friction drag coefficient. In this work, however, the goal is to use the newly calibrated relation instead of the Mack's relation while still using the experimental value of the freestream turbulence intensity, i.e., $Tu = 0.03\%$. This value of FSTI is equivalent to a critical amplification factor of $N_{crit} = 8.87$ according to our new relation [Eq. (22)].

The drag polar for the S809 airfoil at $Re = 2 \times 10^6$ and $M = 0.1$ for an AoA sweep between $[-8, +12]$ deg is shown in Fig. 18. While, in general, the SA-AFT transitional results have consistently increased the accuracy of the lift and drag predictions compared to the fully turbulent solutions (obtained via SA-neg model), the agreements with the experimental data are slightly improved when the newly calibrated relation is utilized. As a matter of fact, the transitional solutions based on the higher critical amplification factor, i.e., $N_{crit} = 11.04$, lead to more underpredictions of the friction drag coefficient compared to the experimental data. Using a lower critical amplification factor, which is attainable via the newly calibrated relation, the friction drag predictions are improved. This results in better agreements with the experimental data, especially in the drag bucket region. It must be noted that such behavior was expected as the reduction of the critical amplification factor results in the expedition of the transition onset that leads to a slight increase in the total drag count. Also shown in Fig. 18 are the fully turbulent and transitional results of Coder [15] using the NASA OVERFLOW 2.2n solver [48] for the same test case with the Medium level (L3) grid utilized. While results are in very good agreement, it must be noted that a critical amplification factor of $N_{crit} = 9.0$ is used for the OVERFLOW results [15]. Interestingly, this value is very close to the critical amplification factor obtained from our newly calibrated relation for the freestream turbulence intensity of 0.03% according to Ref. [45]. It is also important to note that the fully turbulent simulations are not capable of capturing the drag bucket or the low-drag range as they lead to significant overpredictions of the drag count for this airfoil.

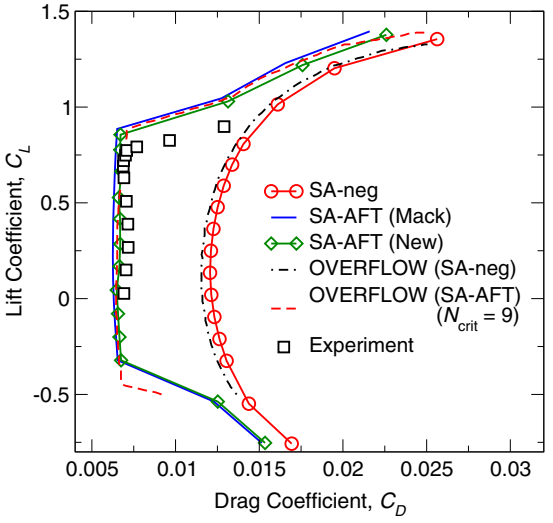

Fig. 18 Drag polar for the turbulent (SA) and transitional (SA-AFT) cases using the original Mack's and the newly calibrated relations: S809 airfoil at $Re = 2.0 \times 10^6$, $M_\infty = 0.1$, and $Tu = 0.03\%$. Experimental data are obtained from Ref. [45] with the OVERFLOW results reproduced from Ref. [15].

Finally, the lift predictions are also plotted against the AoA for the alpha sweep test cases studied in this section. These results are shown in Fig. 19 and exhibit a relatively good agreement with the experimental data in the linear range. However, it must be noted that, similar to the OVERFLOW results, the transitional results are showing slight overpredictions of the lift coefficient, whereas, on the other hand, the fully turbulent simulations are showing slight underpredictions. These small variations in the lift predictions could be mainly attributed to the laminar separation bubble that can create a small region of constant pressure, causing a plateau in the curve of pressure distribution as was seen earlier in Fig. 15. Additionally, fully turbulent cases are leading to a significant underprediction of the pressure profile on the suction side of the airfoil, which also contributes to the underprediction of the lift coefficient, which is dominated by pressure forces. Nonetheless, both fully turbulent and transitional results are significantly overpredicting the maximum lift coefficient as well as the stall angle, which is a known deficiency of the RANS-based turbulence and transition modeling approaches. Once again, these results are in good agreement with those obtained by Coder using the NASA OVERFLOW 2.2n solver [15].

V. Conclusions

A gradient-based optimization approach was utilized for calibrating the critical amplification factor that directly controls the predictive capabilities of transition models based on the linear stability theory, e.g., e^N and the AFT models. For this purpose, four canonical flat plate test cases based on the experimental studies

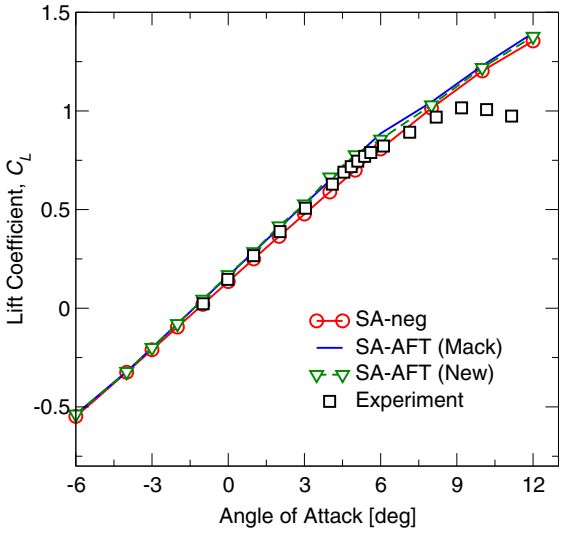

a) Lift versus angle of attack

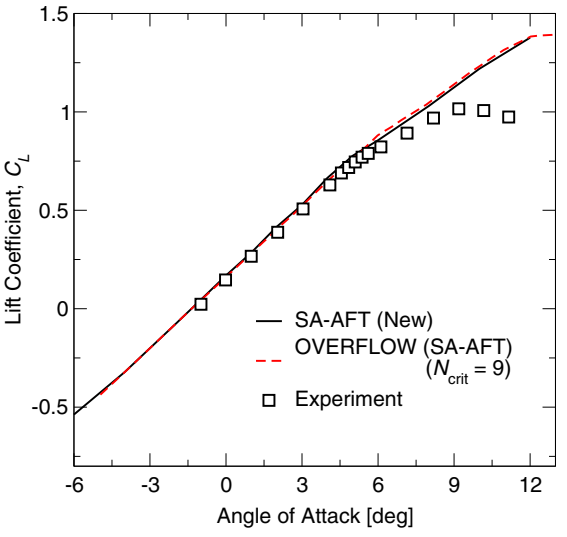

b) Comparison to OVERFLOW results

Fig. 19 Lift predictions for the turbulent (SA) and transitional (SA-AFT) cases using the original Mack's and the newly calibrated relations: S809 airfoil at $Re = 2.0 \times 10^6$, $M_\infty = 0.1$, and $Tu = 0.03\%$. Experimental data are obtained from Ref. [45] with the OVERFLOW results reproduced from Ref. [15].

of the ERCOFTAC T3 series [35] as well as the S&K [36] were considered. Additionally, the transition onset location was represented by a sigmoid function of the turbulence index profile that resulted in a smooth and differentiable design space that is essential to the discrete adjoint approach. Therefore, the critical amplification factor in the source term of the intermittency equation is calibrated via an adjoint-based optimization of the transition onset location based on the experimental data. It must be noted that this work is part of a grand research project focused on uncertainty quantification and calibration of the turbulence and transition models. While other gradient or even non-gradient-based optimization techniques could be used for the present calibration problem with a single design variable involved, the adjoint method is specifically utilized in this work because the adjoint analysis is instrumental to determining the overall uncertainty quantification and sensitivity analysis of the RANS-based transition modeling. Therefore, the adjoint method is also used for obtaining the adjoint flowfields that exhibit the flow reversal and the adjoint flow features. To the best of the authors' knowledge, this was the first work that addressed the calibration of the critical amplification factor using a gradient-based approach that could efficiently identify the N_{crit} values for various bypass and natural transitional test cases. Ultimately, a regression model approach was used to determine a new relation for determining the critical amplification factor as a function of the free-stream turbulence intensity for a wide range of FSTI values. Finally, the efficacy of the newly calibrated relation was verified by modeling the transitional boundary layer of the natural laminar flow NLF(1)-0416 as well as the S809 wind turbine airfoils in a wide range of angles of attack. For the NLF(1)-0416 airfoil, results showed significant improvements in predicting the transition onset location as well as lift and drag coefficients compared to those obtained from the original Mack's relation [3,12]. Additionally, for the S809 wind turbine airfoil, the agreements with the experimental results are improved compared to the transitional flow predictions using the original Mack's relation. More specifically, the newly calibrated relation results in a slower transition at moderate angles of attack, which leads to a slight increase in the friction drag coefficient that enhances the agreements especially in the drag bucket region.

Acknowledgments

This material is based upon work supported by the National Science Foundation under Grant No. CBET-1803760. The authors greatly appreciate the support provided. The authors would also like to thank Coleman Floyd for his contributions to an earlier version of this work that was presented at the AIAA Aviation 2021 conference.

References

[1] Smith, A. M. O., "Transition, Pressure Gradient and Stability Theory," Douglas Aircraft Co. Rept. ES 26388, Santa Monica, CA, 1956.

[2] van Ingen, J., "A Suggested Semi-Empirical Method for the Calculation of the Boundary Layer Transition Region," Technische Hogeschool Delft, Rapport VTH-74, Vliegtuigbouwkunde, Delft, The Netherlands, 1956.

[3] Mack, L., "Transition and Laminar Instability," Jet Propulsion Lab., California Inst. of Technology JPL Publication 77-15, Pasadena, CA, 1977.

[4] Djeddi, R., Coder, J. G., and Ekici, K., "Adjoint-Based Uncertainty Quantification and Sensitivity Analysis of the AFT Transition Model," *AIAA Journal* (under review).

[5] Langtry, R. B., and Menter, F. R., "Correlation-Based Transition Modeling for Unstructured Parallelized Computational Fluid Dynamics Codes," *AIAA Journal*, Vol. 47, No. 12, 2009, pp. 2894–2906. https://doi.org/10.2514/1.42362

[6] Menter, F. R., Smirnov, P. E., Liu, T., and Avancha, R., "A One-Equation Local Correlation-Based Transition Model," *Flow, Turbulence and Combustion*, Vol. 95, No. 4, 2015, pp. 583–619. https://doi.org/10.1007/s10494-015-9622-4.

[7] Bas, O., Cakmakcioglu, S. C., and Kaynak, U., "A Novel Intermittency Distribution Based Transition Model for Low-Re Number Airfoils," AIAA Paper 2013-2531, 2013. https://doi.org/10.2514/6.2013-2531

[8] Menter, F. R., Kuntz, M., and Langtry, R., "Ten Years of Industrial Experience with the SST Turbulence Model," *Turbulence, Heat and Mass Transfer*, Vol. 4, No. 1, 2003, pp. 625–632.

[9] Spalart, P., and Allmaras, S., "A One-Equation Turbulence Model for Aerodynamic Flows," AIAA Paper 1992-0439, 1992. https://doi.org/10.2514/6.1992-439

[10] Barrouillet, B., Laurendeau, E., and Yang, H., "On the Calibration of the Transitional k-ω-γ-$Re_{\theta t}$ Turbulence Model," AIAA Paper 2021-0629, 2021.

[11] Lee, B., and Baeder, J. D., "Prediction and Validation of Laminar-Turbulent Transition Using SA-γ Transition Model," AIAA Paper 2021-1532, 2021.

[12] Drela, M., "MISES Implementation of Modified Abu-Ghannam/Shaw Transition Criterion (Second Revision)," Massachusetts Inst. of Technology, Dept. of Aeronautics and Astronautics, Computational Aerospace Science Lab., Cambridge, MA, 1998.

[13] Coder, J., "Standard Test Cases for Transition Model Verification and Validation in Computational Fluid Dynamics," AIAA Paper 2018-0029, 2018.

[14] Coder, J. G., and Maughmer, M. D., "Computational Fluid Dynamics Compatible Transition Modeling Using an Amplification Factor Transport Equation," *AIAA Journal*, Vol. 52, No. 11, 2014, pp. 2506–2512. https://doi.org/10.2514/1.J052905

[15] Coder, J. G., "Further Development of the Amplification Factor Transport Transition Model for Aerodynamic Flows," AIAA Paper 2019-0039, 2019. https://doi.org/10.2514/6.2019-0039

[16] Coder, J. G., "Enhancement of the Amplification Factor Transport Transition Modeling Framework," AIAA Paper 2017-1709, 2017. https://doi.org/10.2514/6.2017-1709

[17] Denison, M., and Pulliam, T. H., "Implementation and Assessment of the Amplification Factor Transport Laminar-Turbulent Transition Model," AIAA Paper 2018-3382, 2018. https://doi.org/10.2514/6.2018-3382

[18] Coder, J. G., Pulliam, T. H., and Jensen, J. C., "Contributions to HiLiftPW-3 Using Structured, Overset Grid Methods," AIAA Paper 2018-1039, 2018. https://doi.org/10.2514/6.2018-1039

[19] Halila, G. L., Martins, J. R., and Fidkowski, K. J., "Adjoint-Based Aerodynamic Shape Optimization Including Transition to Turbulence Effects," *Aerospace Science and Technology*, Vol. 107, Dec. 2020, Paper 106243. https://doi.org/10.1016/j.ast.2020.106243

[20] Shimoda, M., Azegami, H., and Sakurai, T., "Numerical Solution for Min-Max Shape Optimization Problems: Minimum Design of Maximum Stress and Displacement," *JSME International Journal Series A Solid Mechanics and Material Engineering*, Vol. 41, No. 1, 1998, pp. 1–9. https://doi.org/10.1299/jsmea.41.1

[21] Poon, N. M., and Martins, J. R., "An Adaptive Approach to Constraint Aggregation Using Adjoint Sensitivity Analysis," *Structural and Multidisciplinary Optimization*, Vol. 34, No. 1, 2007, pp. 61–73. https://doi.org/10.1007/s00158-006-0061-7

[22] Abu-Ghannam, B., and Shaw, R., "Natural Transition of Boundary Layers —The Effects of Turbulence, Pressure Gradient, and Flow History," *Journal of Mechanical Engineering Science*, Vol. 22, No. 5, 1980, pp. 213–228. https://doi.org/10.1243/JMES_JOUR_1980_022_043_02

[23] Wang, Y., Zhang, Y., Li, S., and Meng, D., "Calibration of a γ-Re_θ Transition Model and its Validation in Low-Speed Flows with High-Order Numerical Method," *Chinese Journal of Aeronautics*, Vol. 28, No. 3, 2015, pp. 704–711. https://doi.org/10.1016/j.cja.2015.03.002

[24] Colonia, S., Leble, V., Steijl, R., and Barakos, G., "Assessment and Calibration of the -Equation Transition Model at Low Mach," *AIAA Journal*, Vol. 55, No. 4, 2017, pp. 1126–1139. https://doi.org/10.2514/1.J055403

[25] Abd Bari, M. A., Da Ronch, A., Panzeri, M., and Drofelnik, J., "On the Calibration of the Intermittency Transition Turbulence Model for Wind Turbine Airfoil by Machine Learning Algorithm," *31st Congress of the International Council of the Aeronautical Sciences*, International Council of the Aeronautical Sciences (ICAS), Bonn, Germany, 2019.

[26] Nader, G., dos Santos, C., Jabardo, P. J., Cardoso, M., Taira, N. M., and Pereira, M. T., "Characterization of Low Turbulence Wind Tunnel," *XVIII IMEKO World Congress*, International Measurement Confederation (IMEKO), Budapest, Hungary, Sept. 2006.

[27] Scheiman, J., and Kubendran, L., "Laser Velocimeter Measurements in a Wing-Fuselage Type Juncture," NASA TP 100588, 1988.

[28] Coder, J. G., "Development of a CFD-Compatible Transition Model Based on Linear Stability Theory," Ph.D. Thesis, Pennsylvania State Univ., State College, PA, 2014.

[29] Shi, Y., Mader, C. A., He, S., Halila, G. L., and Martins, J. R., "Natural Laminar-Flow Airfoil Optimization Design Using a Discrete Adjoint Approach," *AIAA Journal*, Vol. 58, No. 11, 2020, pp. 4702–4722. https://doi.org/10.2514/1.J058944

[30] Smith, A., and Gamberoni, N., "Transition, Pressure Gradient and Stability Theory," Douglas Aircraft Rept. ES-26388, 1956.

[31] Stefanski, D. L., Glasby, R. S., Erwin, J. T., and Coder, J. G., "Development of a Predictive Capability for Laminar-Turbulent Transition in HPCMP CREATE-AV Kestrel Component COFFE Using the Amplification Factor Transport Model," AIAA Paper 2018-1041, 2018.

[32] Allmaras, S. R., and Johnson, F. T., "Modifications and Clarifications for the Implementation of the Spalart-Allmaras Turbulence Model," *7th International Conference on Computational Fluid Dynamics (ICCFD7)*, International Conference on Computational Fluid Dynamics (ICCFD) Paper ICCFD7-1902, 2012, pp. 1–11.

[33] Djeddi, S., "Towards Adaptive and Grid-Transparent Adjoint-Based Design Optimization Frameworks," Ph.D. Thesis, Univ. of Tennessee, Knoxville, TN, 2018.

[34] Djeddi, R., and Ekici, K., "FDOT: A Fast, Memory-Efficient and Automated Approach for Discrete Adjoint Sensitivity Analysis Using the Operator Overloading Technique," *Aerospace Science and Technology*, Vol. 91, Aug. 2019, pp. 159–174. https://doi.org/10.1016/j.ast.2019.05.004

[35] Coupland, J., "ERCOFTAC Special Interest Group on Laminar to Turbulent Transition and Retransition: T3A and T3B Test Cases," European Research Community on Flow, Turbulence, and Combustion (ERCOFTAC) TR A309514, Bushey, U.K., 1990.

[36] Schubauer, G. B., and Klebanoff, P. S., "Contributions on the Mechanics of Boundary-Layer Transition," National Advisory Committee For Aeronautics TN 3489, Washington, D.C., 1956.

[37] van Ingen, J., "The eN Method for Transition Prediction: Historical Review of Work at TU Delft," AIAA Paper 2008-3830, 2008. https://doi.org/10.2514/6.2008-3830

[38] Cakmakcioglu, S. C., Bas, O., and Kaynak, U., "A Correlation-Based Algebraic Transition Model," *Proceedings of the Institution of Mechanical Engineers, Part C: Journal of Mechanical Engineering Science*, Vol. 232, No. 21, 2018, pp. 3915–3929. https://doi.org/10.1177/0954406217743537

[39] Djeddi, R., Floyd, C. D., Coder, J. G., and Ekici, K., "Adjoint-Based Uncertainty Quantification and Calibration of RANS-Based Transition Modeling," *AIAA AVIATION Conference*, AIAA Paper 2021-3036, 2021. https://doi.org/10.2514/6.2021-3036

[40] Somers, D. M., "Design and Experimental Results for a Natural-Laminar-Flow Airfoil for General Aviation Applications," NASA TP 1861, 1981.

[41] Brophy, C. M., "Turbulence Management and Flow Qualification of the Pennsylvania State University Low-Turbulence, Low-Speed, Closed-Circuit Wind Tunnel," Ph.D. Thesis, Pennsylvania State Univ., State College, PA, 1994.

[42] Premi, A., Maughmer, M., and Brophy, C., "Flow-Quality Measurements and Qualification of the Pennsylvania State University Low-Speed, Low-Turbulence Wind Tunnel," AIAA Paper 2012-1214, 2012. https://doi.org/10.2514/6.2012-1214

[43] Van Ingen, J., Boermans, L., and Blom, J., "Low-Speed Airfoil Section Research at Delft University of Technology," *12th Congress of the International Council of the Aeronautical Sciences*, International Council of the Aeronautical Sciences (ICAS), Bonn, Germany, 1980.

[44] Usah, W., Jr., and Murman, E., "Embedded Mesh Solutions of the Euler Equation Using a Multiple-Grid Method," AIAA Paper 1983-1946, 1983.

[45] Somers, D. M., "Design and Experimental Results for the S809 Airfoil," National Renewable Energy Lab. TR NREL/SR-440-6918, Golden, CO, 1997.

[46] Brodeur, R. R., and Van Dam, C., "Transition Prediction for a Two-Dimensional Reynolds-Averaged Navier–Stokes Method Applied to Wind Turbine Airfoils," *Wind Energy: An International Journal for Progress and Applications in Wind Power Conversion Technology*, Vol. 4, No. 2, 2001, pp. 61–75. https://doi.org/10.1002/we.47

[47] Medida, S., and Baeder, J. D., "Application of the Correlation-Based γ-$Re_{\theta t}$ Transition Model to the Spalart-Allmaras Turbulence Model," AIAA Paper 2011-3979, 2011.

[48] Buning, P., and Nichols, R., *User's Manual for OVERFLOW 2.2*, NASA Langley Research Center, Hampton, VA, 2010.

C. Lee
Associate Editor